technical memorandum

Daresbury Laborator

DL/SCI/TM66E

A REIVEW OF THE POWDER DIFFRACTION PROJECT JANUARY - JUNE 1988

by

R.J. CERNIK, SERC Daresbury Laboratory.

MARCH, 1990

G90/84

Science and Engineering Research Council
DARESBURY LABORATORY
Daresbury, Warrington WA4 4AD

ISSN 0144-5677

SCIENCE AND ENGINEERING RESEARCH COUNCIL
DARESBURY LABORATORY

A REVIEW OF THE POWDER DIFFRACTION PROJECT JANUARY - JUNE 1988

By R J CERNIK

SECTION A

STATION 9.1

The station has been substantially rebuilt, there is a new front end and monochromator assembly, the working area outside the hutch has been re-designed, the diffractometer drive system has been replaced and several new detectors including a curved position sensitive detector have been acquired. The station was ready for commissioning on 20 January 1988, unfortunately a series of vacuum and shutter problems on 9.1 have meant that only 120 shifts from a possible 248 have been useable up to the end of the first scheduling period in 1988. During these 120 shifts the following projects have been undertaken:

1. Si(111) monochromator test
2. Wavelength scanning
3. Structural studies of zeolites
4. Analysis of the line broadening standards BaF_2 and LaB_6
5. Data collection for Rietveld refinement for three samples of Bi-Sr-Ca-Cu High T_c superconductors.
6. Studies of the kinetics of ordering processes in minerals
7. Preliminary in situ electrochemistry experiments
8. Studies of amorphous materials using anomalous dispersion
9. Phase transition and kinetics of the Kaolinite - meta Kaolinite transformation using a furnace and curved position sensitive detector
10. Characterisation of CdTe-InSb surface structures.

1. Monochromator tests

Principal Investigator: R J Cernik

A channel cut Si(111) monochromator has been used as the standard on station 9.1 for the past three years. After the new front end was completed the intensity output from the monochromator was monitored as a function of time as the shutter was opened and closed. Fig 1 shows the results. It can be clearly seen that immediately after the shutter is opened the intensity drops rapidly by 25%. The amount of intensity loss depends upon the size of the polychromatic beam that is incident on the first monochromator crystal. The monochromator angle also changes the specific heat loading on the crystal, the larger the angle (ie longer wavelength) the more marked the effect. The heating effects can be reduced by backfilling the monochromator vessel with He gas and by using a very small beam size. However the original design concept of the station was for a wide incident beam on the monochromator crystal so that the wavelength could be changed without altering the height of the monochromatic beam defined by the fine exit slits.

A water cooled channel cut monochromator has been designed and built by M Hart and will be installed and tested in late July 1988. This monochromator should significantly benefit those users working with wavelength longer than 1.2Å.

2. Wavelength scanning

Principal Investigators: P Adams, P Hatton, H Jahns ABTAT 241

The energy resolution of a conventional energy dispersive experiment using polychromatic radiation is detector limited. A method of achieving a higher energy resolution is to maintain the specimen and detector at a fixed angle, and to vary the monochromator angle in fine steps. The energy resolution is then limited by the accuracy of the monochromator drive system.

A preliminary attempt to evaluate this technique was carried out on 9.1 using Indium Iodide. Fig 2 shows the unnormalised results from this specimen, the beam size was (0.7 x 5)mm, the detector angle was fixed at 15° 2θ, the detector receiving slit was set to 0.5mm, the counting time was 1 second per point, and the monochromator steps size was 4 m deg, giving an approximate energy resolution of 4eV. The total data collection time was 2½ hours and covered the energy range 8.7-28 KeV. The monitor count for this run is shown in Fig 3. The increase in intensity follows the synchrotron profile. In addition approximately 44 multiple reflection "glitches" can be seen.

The energy dispersive technique is particularly useful when using environmental cells with limited angular apertures such as a diamond anvil cell. Such cells require very small beam cross sections, typically 100μm in diameter. If we were to use a comparable beam size in the wavelength scanning mode the intensity would drop by a factor of approximately 350. With the current experimental design on 9.1 a typical wavelength scan through a diamond anvil cell with a beam cross section of $100\mu m^2$ would take approximately thirty days even for a modest energy range. This technique is therefore currently only suitable for use on an environmental cells that can transmit or reflect beams of a similar size to those used in the conventional monochromatic angular scans.

3. Structural studies of zeolites

Principal Investigators: A M Glazer, L B McCusker, also Shell Amsterdam

Several groups both from academic and industrial backgrounds are interested in the possibility of solving crystal structures ab initio from powder diffraction data. This is necessary since many industrially and chemically important substances cannot be grown as single crystals large or pure enough for conventional Laboratory four circle methods; Examples are many of the new high T_c oxide superconductors, zeolites and industrial multi phase catalysts.

The experimental arrangement on 9.1 for high resolution powder diffraction consists of a diffractometer in Debye-Scherrer geometry with a large specimen - detector distance (640mm). The specimen is mounted in a thin walled capillary tube which is bathed with the incident radiation. The diffracted beam passes through a double slit and evacuated beam pipe assembly before the signal is detected. The detector is usually a high resolution Harshaw NaI(Tl) scintillation counter, but solid state detectors and proportional counters are also available.

Fig 4 shows a spectrum collected on 9.1 for silicalite, a zeolite with a complex but known structure. The diffraction pattern shown here has been normalised for beam decay and has had the background subtracted. Automatic peak finding (using a second derivative algorithm) followed by autoindexing (P E Werner's TREOR) led directly to the correct unit cell.

The critical step in the data processing is the extraction of accurate reflection intensities from the powder diffraction profile. This was

accomplished with a modified version of Pawley's ALLHKL program. The program does a whole-pattern refinement of all symmetry-allowed reflection intensities (assuming a Gaussian peak shape), the unit cell parameters, the 2θ zero correction, and the FWHM function. For Debye-Scherrer geometry with a simple slit system, a Gaussian peak shape is quite valid and describes the test example peaks well.

Fig 4 shows the raw data, the calculated fit, the residual intensity and the peak positions. It can be seen that even when seven peaks overlap to give only two distinguishable peaks at $2\theta = 22.5°$ a good fit can be achieved. The residual is due mainly to the non Gaussian nature of the peak tails. Hence a modification to the code to include the peak shapes is planned.

Once a set of indexed peaks is obtained together with a set of integrated intensities a structural solution can be attempted.

Data were collected from a zeolite (ZP88) with an unknown structure, parts of the data collection are shown in Figs 5 and 6. A major problem with zeolites is that they are poor scatterers and the data rapidly falls off with increasing angle. The peaks shown in Fig 5 are well resolved having peak halwidths of 0.065°. Fig 6 shows the same data set at higher angles, the structural information is still present with the synchrotron data although of reduced statistical significance. The best laboratory results so far on this compound using the Stoe high resolution system do not show any detail of quality above $2\theta \approx 40°$. This compound is currently being analysed.

Once a physically and chemically sensible structural model has been obtained, the structure may be refined either by conventional least squares or by using the method of Rietveld. This is a whole pattern refinement technique for which a comprehensive suite of programs has been developed by Drs A D Murray and A N Fitch.

4. Line broadening studies

Principal Investigator: J I Langford

BaF_2 and LaB_6 are possible candidates for an international line-broadening standard. While the BaF_2 gives slightly sharper lines than the LaB_6 with a conventional diffractometer ($\lambda = 0.7$Å Cu Kα), the line

breadths from 9.1 (λ = 0.7Å) are essentially the same. This suggests that the differences observed previously are due to small differences in absorbtion at the longer wavelength and are not due to residual intrinsic broadening with LaB_6.

The quality of the high resolution data from 9.1 is excellent, especially for BaF_2, the full data set is shown in fig 7. The peaks fit well to either a Voight or pseudo Voight function. Fig 8 shows the 420 peak fitted with the latter, the FWHM is 0.031°, the mixing parameter is 0.3, and the peak position was found to be better than 1×10^{-4} degrees.

The full width half maximum function has a minimum value of 0.03° (2θ) at 20-25° (2θ) for both samples (figs 9 and 10), and there is little variation in the integral breadth (β) over the range scanned. Sample broadening is evidently very small or negligible. A preliminary analysis of peak shapes for LaB_6 indicates that the profiles are intermediate between a Gaussian and a Lorentzian, and tend towards the latter as 2θ increases. If Voight functions are assumed, the Gaussian component is essentially constant over a wide range of angle, but increases at low angle due to axial divergence. Fig 11 shows the integral breadths (β) and the Gaussian (β_G) and Lorentzian (β_L) components of the Voight function for LaB_6. Fig 12 shows the equivalent results for BaF_2. The Gaussian components for both specimens are constant with 2θ, except for the axial divergance component, which could in future be removed, either by using a narrower incident beam or by using Soller slits. Fig 13 shows the increase in the Lorentzian component of both specimens. This is approximately linear with 2θ but increases more rapidly for LaB_6. This indicates that the resolution function of the instrument is not the major component of the line width.

Both data collections were punctuated with port closures due to beam line vacuum failures. The counting times for both experiments were therefore not sufficiently long to produce data of the highest statistical quality. This can be seen in the spread of points on the LaB_6 data compared with the BaF_2 on figs 9 and 10.

However the initial analysis of the data collected during this period indicates that these data have the best resolution yet seen in Debye-Scherrer geometry, coupled with a high count rate and symmetric peak

shapes. For the future it is planned to collect more data on a fewer number of peaks over a wider 2θ range in order to improve the quality of the counting statistics. Coupled with the already excellent angular resolution. Station 9.1 will offer excellent opportunities for the quantitative analysis of polycrystalline materials.

5. High T_c superconductors
Principal Investigators: J I Langford and W I F David

One sample of a Bi-Sr-Ca-Cu superconductor was prepared at Birmingham and two were prepared at the Rutherford Appleton Laboratory. Two of three datasets were suitable for further processing - and Rietveld refinement showed that both have the same structure as $Bi_2\ SR_2\ Ca\ Cu_2\ O_8$. R factors are as follows

	Rp %	Rwp %	Re %
Birmingham sample	7.9	9.9	6.3
RAL sample	10.0	13.0	6.1

The results of the RAL refinement were presented at the British crystallographic meeting at Warwick 1988.

6. The Kinetics of Ordering Processes in Minerals
Principal Investigators: E Salje, S Redfern and A Graeme-Barber

Disorder and strain are of fundamental importance to the energetics of crystal minerals. Ideas previously applied to the understanding of thermodynamic equilibrium states of minerals undergoing phase transitions are now being extended by Salje and co-workers to the problems of off-equilibrium kinetic behaviour. Two mineral systems have recently been investigated by high resolution powder diffraction at beamline 9.1.

a) <u>Hexagonal-Orthorhombic transition in Cordierite</u>

Splitting of the 211 hexagonal Bragg peak in cordierite (a framework mineral) has already been employed as a measure of the strain order parameter, Q. The structural distortion is found to be a function of annealing time for hexagonal material crystallized from glass in the

orthorhombic stability field. Recent study has focussed on the role of cation substitution on the kinetic and structural behaviour at this phase transition. A suite of potassium bearing cordierites annealed for various times has revealed that the introduction of potassium reduces the maximum spontaneous strain associated with the distortion although the kinetic behaviour is otherwise similar to that in pure Mg-cordierite. The potassium introduces local strain fields which act as the conjugate field to the order parameter Q. previous interpretations of the effects of potassium were confused due to the lack of resolution of conventional diffractometers. The high resolution results at the SRS have lead to a fuller understanding of the role fo cation substitution in relation to the conjugate field.

b) Al/Si Ordering in Na-feldspar

The kinetics of Al/Si ordering within the tetrahedral framework of Albite (Na-feldspar) hae been investigated by means of observation of the changes in the 131 powder line as a function of annealing time for a series of partially disordered samples. The line profile represents a power spectrum of the states or order, Q_1, in a sample. For the first time a kinetic pathway has been correlated with a sequence of progressively inhomogeneous states of order finally converging on a homogeneously ordered sample ($Q_1 = 1$). This exciting result ties in with an approach to the kinetics of ordering which applies Landau theory to off-equilibrium time dependent processes, and provides the first supportive evidence for this approach. Again, the fine changes in line profile have been observed with the aid of high resolution scans over a small 2θ range at the powder diffractometer.

Fig 14 shows the theoretical prediction for the evolution of the order parameter as a function of time. Four synchrotron runs on specimens that were annealed for 5, 21, 46 and 64 days are also shown. These can be seen in more detail in Fig 15. Graph 1 corresponds to the specimen that was annealed for 5 days, 2 - 21 days, 3 - 46 days and 4 - 64 days. Spectrum 4 has the true background value, the other spectra have had 1000 counts successively added for clarity in the diagram.

7. Preliminary in-situ electrochemistry

Principal Investigators: S J Doyle and K Roberts

Studies of Zn and ZnFe phosphate formation on steel surfaces

Initial studies in the electrochemistry programme have centred on the formation of films of zinc and zinc-iron phosphates on steel. It is known that such films provide corrosion protection to the steel, and this effect is almost universally used in the motor industry to protect car bodies prior to painting. Due to technical problems with the in-situ cell the studies reported at present were carried out 'ex-situ', on samples which were prepared immediately prior to X-ray characterisation. It is hoped in forthcoming beamtime to extend these measurements to in-situ characterisation.

The two phosphates of interest in corrosion inhibition are the zinc phosphate hydrate $Zn_3(PO_4)_2.4H_2O$, and the zinc-iron phosphate hydrate $Zn_2Fe(PO_4)_2.4H_2O$. Both these salts occur naturally as the minerals hopeite and phosphophyllite respectively, and it has been shown that the effectiveness of corrosion inhibition is determined by the ratio of both phosphates, and not by the presence of either one alone. Normally the process of phosphating is carried out in a solution of phosphoric acid containing the required amounts of iron and zinc salts. In this way a relatively constant proportion of both phosphates is formed. The reaction is normally carried out at 'rest potential', ie under open circuit conditions, and the product is a mixture of both hopeite and phosphophyllite, but it is also possible to drive the reaction electrochemically to produce an excess of one or other of the salts; for example cathodic deposition, where the steel is at a negative potential with respect to the reference electrode, gives a hopeite rich phosphate deposit, while anodic deposition gives a phosphophyllite rich surface layer.

An initial examination of the effect of varying potential on the formation of the phosphate layer clearly illustrates that the deposition product is potential dependent. Figure 15(a) shows both the observed and predicted powder diffraction patterns for three different cases, the first (a) being for deposition under cathodic conditions, where we expect the product to be mainly hopeite, then (b), deposition under normal open circuit conditions, where a mixture of hopeite and phosphophyllite is

expected, and finally (c), deposition at anodic potential, where the product should be mainly phosphophyllite. The strong similarities between the predicted and observed patterns demonstrates the role of electrochemical control in the nature of the product.

It has also been possible to observe the development of the phosphate film as a function of exposure time to the phosphating solution, and the results, illustrated in figure 15(d), shows that even after times as short as a few seconds it is possible to detect the presence of the phosphate layer on the steel substrate. Detection of crystallisation in this early stage is of importance in relation to the adhesive properties and stability of the deposited crystalline phases.

8. Studies of amorphous materials using anomalous scattering
Principal Investigators: Professor J Finney and Dr G Bushnell-Wye

Progress was made recently in the development of experiments which exploit anomalous scattering to study amorphous and poorly-crystalline substances. A group from Birkbeck College are collaborating in a CASE award with BP to investigate materials in which catalyst particles, present in only a few percent by weight, are supported by inert substrates. Although the refurbished station was not fully optimised for this type of study, and despite beam injection problems following a short shutdown, with the improved flux now available on this station it was possible to demonstrate clearly the anomalous scattering by the metal component and these effects confirmed the presence of other compounds. The higher Q range achieved provided additional data and better spacial resolution whereas, perhaps more significantly, the improved signal to noise ratio greatly increase the chances of obtaining reliable quantitative details of the particles' shape and size from peak profile analysis.

A four bounce monochromator system, based upon a free flex flexural pivot design will soon be ready for operation. This monochromator configuration will reduce the $\delta\lambda/\lambda$ distribution in the main beam, and also improve the control stability driving in close to an absorbtion edge. In addition the new water cooled monochromator will be available from July 1988 and this will significantly increase the intensity available especially at the Ni edge.

(Example)

X-ray Anomalous Diffraction Study of Aqueous $NiCl_2$.

A. J. Dent,[1,2] P. S. Jarrett,[3] A. G. Orpen[3]

[1]Daresbury Laboratory, Daresbury, Warrington WA4 4AD.
[2]Department of Chemistry, University of Manchester, Manchester M13 9PL.
[3]Department of Inorganic Chemistry, University of Bristol, Bristol BS8 1TS.

The study of the structure of complex disordered systems by x-ray diffraction has traditionally been hampered by the one-dimensional data that can be measured. Typically a single x-ray wavelength is employed and a total structure factor $S(q)$ ($q = 4\pi \sin\theta/\lambda$) is derived from the coherent diffracted intensity as a function of scattering angle (2θ). From $S(q)$, a radial distribution function $G(r)$ may be derived by a Fourier transform. Use of multiple x-ray wavelengths, measuring $S(q)$ as a function of x-ray energy close to an absorption edge, where substantial changes in scattering factor occur, may lead to enhanced structural information.

Our first study using synchrotron radiation on station 9.1 at the SRS enabled us to obtain the difference structure factor $\Delta S(q)$ and corresponding difference radial distribution function $\Delta G(r)$ for the nickel environment. However, the results were limited by poor signal to noise [1]. We have recently recollected the data after the modifications to station 9.1 and a comparison of the old (top) and new (bottom) raw data are shown below. The improved signal to noise ratio is quite evident, although part of this is due to a twofold increase in sample size. The detailed differences between the spectra are due to a different sample holder.

We are confident that the improved data will lead to a greater understanding of the structure of aqueous $NiCl_2$, although improvements to the stability of the monochromator are required to allow the x-ray energy to be defined accurately.

[1] A. J. Dent (1988) *Ph. D. Thesis*, Bristol University, in print.

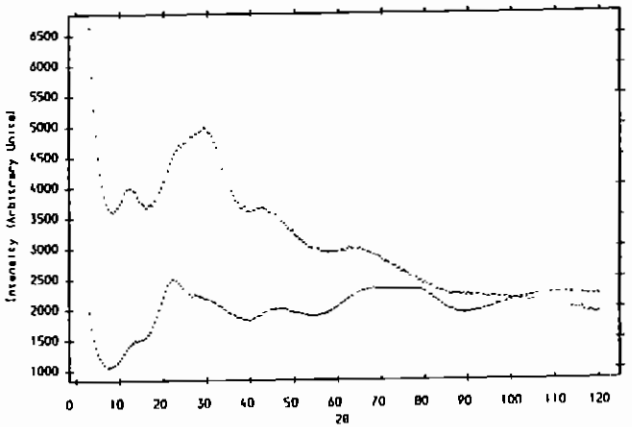

Figure 1: The raw diffracted intensity from 4.2 molal aqueous $NiCl_2$ at an x-ray energy of 8.04 keV (≈ 300 eV below the Ni K-edge) pre (top) and post (bottom) the modifications to station 9.1.

9. Phase Transition and Kinetics of the Kaolinite - meta kaolinite Transformation using a Furnace and Curved Position Sensitive Detector
Principal Investigators: P Barnes, S Tarling, S Clark, J Jones, R Cernik and E Dooryhee

The kaolinite - meta kaolinite transformation is the central transformation in many industrial processes involving the calcining of clay materials and furnacing or hydrothermal activation of alumino silicates. The structure of kaolinite has now been solved using a combination of X-ray and neutron diffraction, but the meta - kaolinite structure being semi or completely amorphous has not been adequately modelled. It is important to model however since the industrial energy cost of the transformation is high and the crystal chemistry is still unresolved.

The reaction temperature is approximately 585°C, the kaolinite specimen was therefore mounted in the newly acquired GTP furnace. This is shown in Fig 16, the sample is mounted in a flat plate specimen holder (2) which is rotatable through a gear mechanism in the furnace mount (3). The incident X-ray beam from the monochromator vessel emerges (4) and falls on the specimen. The diffracted pattern is recorded by an Inel curved position sensitive detector (1) with a 120° aperture. The detector is mounted on the diffractometer 2θ arm (5), the detector can therefore also be scanned. Fig 17 shows the furnace with the cover (1) and heating element in place ready for use. A beryllium window (2) allows the incident beam in and the diffracted beam out. The jacket is water cooled (3) and the heater element is supplied through cables (4) from a transformer in the hutch. The maximum tested temperature for the furnace as measured with the internal K type thermocoupler is 800°C at a pressure of 5.1×10^{-4} torr. A full temperature calibration with standard specimens still remains one of the immediate priorities for the furnace. There was insufficient time to carry this out during the current run, the information collected on the transition is therefore qualitative. The neutronic controller provided satisfactory temperature stability with a short response time. The oscillation of ±0.5°C in a ramping segment was acceptable even when heating as fast as 25°C/min, however the ramping is less smooth below 100°C. The control over a dwell segment is good with typically a small overshoot of 1°C and a negligible temperature drift.

A summary of the position sensitive detector is given in Appendix I written by Dr G Bushnell-Wye. One of the problems associated with using a detector with such a large aperture is that scattering from many sources is seen and detected. Two examples of peaks extraneous to the specimen are the scattering from the Be window on the end of the beam pipe, and the scattering from the Be window on the furnace. A number of possible solutions are being investigated, including replacing the Be with amorphous Kapton foil, and building a set of radial Soller slits.

Fig 18 shows the Kaolinite - meta kaolinite transformation, the temperature scale on the right is in degrees C but is uncalibrated. The onset of the phase transition is known to occur approximately 80° higher. However the transition can clearly be seen. The semi amorphous stage appears to have been reached by the 8th spectra. The small peak on the left hand side is due to a Be window. Data collection times were 300s per spectrum and the statistical specimen is good even in the amorphous phase. The possibilities for Kinetics work on 9.1 have therefore been considerably improved by the addition of the Inel position sensitive detector.

10. Characterisation of CdTe-InSb superlattices
Principal Investigators: J E MacDonald, K Conway, R Hine and R Potter

There is considerable current interest in the use of single and multilayer structures of the narrow bandgap semiconductors CdTe and InSb as infra-red detectors. Their use in practical devices is however limted by the quality of the interface between the two materials. As part of a collaboration between University College Cardiff, RSRE Malvern and Night Vision we are employing a laboratory-based double crystal diffractomer and the powder diffraction station at Daresbury to investigate the quality of CdTe-InSb heterojunctions and superlattices grown by molecular beam epitaxy. Scans of the (004) and (006) peaks (figs 18(a) and 18(b) respectively) of a period superlattice of 900Å CdTe - 900Å InSb display a series of fringes arising from the coherent interference between the periodic layers, in addition to the substrate Bragg peak. These fringes are observed for superlattices composed of layers of thickness greater than 200Å. However, for thinner layers, the substrate peak together with a broad CdTe peak are observed, indicating that ordered, discrete crystalline layers are not formed. This may be due to either a chemical reaction or roughness at the interface. Further investigation using Transmission Electron Microscopy is in progress.

SECTION B

STATION 8.3

Principal Investigators: A N Fitch, R Cernik, P Pattison and C R A Catlow

The new high-resolution diffractometer at station 8.3 is situated on a bending magnet of the storage ring, and is equipped with a channel-cut silicon (111) monochromator, giving a range of X-ray wavelengths from 1-2.5Å. The sample is contained in a rotating flat-plate specimen holder which is being loaded by Dr A N Fitch (see Fig 19), and scanning in either θ/2θ mode or at fixed sample orientation is possible. Owing to the parallel nature of synchrotron radiation in the vertical sense, the resolution of the instrument is controlled by a set of long, fine, diffracted-beam collimators, as described by Parrish and Hart [1]. To enter the detector, photons from the incident beam must fulfil the strict conditions of scattering direction imposed by the collimators, Fig 20. For 8.3, peak widths of about 0.05° are obtained for highly crystalline samples. A coarser set of vertical Soller slits minimises the effects of the axial divergence of the incident radiation, so that well-defined, symmetric peaks are obtained, even down at low angles.

The optics of the instrument ensure that the positions of the diffraction peaks are largely free from a number of systematic and geometric errors which can occur with conventional X-ray diffractometers. The diffractometer is therefore ideally suited to obtaining accurate peak positions for precision lattice parameter measurements. Accurate peak positions are also essential for the determination of the unit cell and for indexing of the patter in ab-initio structure determination from powder data alone. There is increasing interest in direct determination of crystal structure from powder-diffraction data, for the wide range of materials for which single crystals are very difficult or impossible to grow, eg industrial catalysts (which may be multi-component systems) or the new classes of oxide superconductors. The diffractometer is equipped with high-resolution encoders linked directly to the 2θ and sample (ω) axes, with a precision of 0.0001 and 0.001, respectively.

Peak positions have been found to be reproducible to 0.0004°, ie within 2 standard deviations of the average peak position determined by least-squares fitting of an assumed peak-shape function to the diffraction profile, Fig 21. For specific specimens however the peak positions have been found to better than 0.0001°. The diffractometer is driven by D.C. motors with direct feedback from the encoders, so that the detector or the sample may be rapidly driven to any desired angular position. At present, data are collected in the step-scan mode, but modifications are planned to allow continuous scanning, thus leading to more-rapid rates of data acquisition. The excellent signal to noise of the data will be useful in revealing small quantities of crystalline impurity phases in a sample, or for the identification of weak superlattice reflections.

As well as operating in a monochromatic, angle-scanning configuration, the diffractometer can be operated in an energy-dispersive mode. By fixing the detector at a chosen angle (2θ), and by scanning the monochromator through its range of accessible wavelengths (λ), the Bragg condition ($n\lambda = 2d\sin\theta$) can be fulfilled at wavelengths corresponding to the various lattice spacings (d) of the sample. In this way a diffraction pattern can be obtained, with a resolution more than an order of magnitude better than that obtained using the conventional energy-dispersive technique, ie using white radiation and an energy-sensitive detector. The geometry of this arrangement has great advantages when using restricted sample environments, eg a pressure cell with fixed entrance and exit windows.

Although operational for only about two months, a number of important experiments have already been carried out which illustrate the scope and potential for the new diffractometer.

The high intensity of the synchrotron radiation and the flat-plate nature of the sample are ideally suited to experiments on thin, crystalline surface layers. Thus experiments, performed by workers from the University of Kent, on a 5μm layer of lead phthalocyanine on a saphire support showed that the structure of the film is quite different from that of the bulk material. Thin films of metal phthalocyanines exhibit marked changes in their conductivity in the presence of adsorbed gases (eg nitrous oxides NO_x) thus providing the bases for a simple, cheap and highly-sensitive sensor.

A layer of oxide grown on metal substrate can be under considerable stress, owing to the mismatch between the structures of the two components, or to differences in their thermal expansivity. It is recognised that these stresses can plan an important role in the adhesive properties of the film; as to whether it sticks, forming a protective layer, or whether it spalls off, leaving an exposed area where renewed oxidation can occur. The stresses in the layer cause small changes in the spacings of lattice planes as a function of their inclination to the surface of the sample. Thus by observing the change in the position of a diffraction peak with sample orientation, these stresses can be investigated. With 8.3 there are no problems associated with parafocussing, peak broadening or beam penetration as are observed with conventional diffraction geometries. Measurements on layers of NiO (5 - 20 μm) on Ni, (provided by AERE Harwell), showed, from very small splittings of the peaks, that the NiO layer has a rhombohedral structure. Very small, stress-induced peak shifts from 0.001 to 0.04° with sample orientation were easily identifiable owing to the high resolution and precision of the diffractometer drive system.

Data collected on the ulcer drug "Cimetidine", by workers from Chemical Crystallography in Oxford, illustrate the excellent quality of the diffraction patterns that can be obtained, Fig 22. Such data should be suitable for least-squares refinement by the Rietveld method, which calculates a complex diffraction profile as a sum of overlapping peaks of assumed peak shape (eg Gaussian, pseudo-Voight). Peak positions are determined from the refined values of the lattice parameters (and zero point), peak widths follow a simple function of θ, and peak intensities depend on the structure factors and hence on the refined values of the atomic parameters.

Rietveld refinement is being performed on a number of samples of cement, (Birkbeck College, London). Distinction betwen the various proposed structural models for this multi-component system will eventually be possible, leading to a greater understanding of the solid-state chemistry of this important material.

[1] W Parrish and M Hart, Transactions of the American Crystallographic Association, 21, 51, (1985).
M Hart and W Parrish, Materials Science Forum, 9, 39, (1986).

SECTION C

ENERGY DISPERSIVE DIFFRACTION

Principal Investigators: S M Clark, K Roberts, P Barnes, M Hart and C R A Catlow

There has been considerable interest in energy-dispersive powder diffraction (EDPD) since it was first demonstrated [1], using both laboratory [2, 3] and synchrotron sources [4, 5]. Although the main contribution of the technique has been in the field of high pressure research [6, 7] it has also been applied to the study of high [8] and low [9, 10] temperature phase transitions and to structural studies not only of crystalline solids [12], but also amorphous solids [12], liquids [13], and gases [14]. In 1986 a study was carried out on station 9.7 of the SRS to determine if EDPD was practical [15]. A permanent facility was subsequently constructed, and is described in this paper.

The conventional powder diffraction method uses a monochromatic beam of X-rays of wavelength λ and varies the diffraction angle 2θ in order to sample a range of lattice planes of interplanar spacing d.

$$\lambda = 2d\sin\theta$$

In the energy-dispersive method the diffraction angle is kept fixed and a polychromatic beam of X-rays is used. Each set of lattice planes diffracts X-rays of different energy E, as given by:

$$E = \frac{6.199}{d\sin\theta}$$

where E is in keV and d is in Angstroms. The diffracted X-rays are detected by a semiconductor detector, which produces a voltage pulse of magnitude proportional to the X-ray energy. The variation of energy for various reflections of silicon as a function of diffraction angle is shown in Fig 23. Using such a diagram it is possible to select the optimum detector angle for a particular experiment.

The number of counts recorded by the detector at a particular energy and diffraction angle $I(E,\theta)$ is given by [2]:

$$I(E,\theta) = [X(E)*A(E)\cdot T(E,\theta)]*S(E,\theta)*D(E)$$

where X(E) is the distribution of X-ray intensity produced by a wiggler magnet in this case, A(E) is any X-ray absorbtion due to air or beryllium windows, $T(E,\theta)$ is a geometrical aberation function, $S(E,\theta)$ is the scattering from the sample and D(E) is the detector efficiency function. $S(E,\theta)$ is the quantity to be determined but $I(E,\theta)$ is actually measured. Usually an empirical approach is used [5]. The pattern of a standard material is measured and a normalisation curve is calculated from the measured pattern and the expected pattern. However, most energy-dispersive patterns are collected in order to determine lattice constants; for peaks that are not seriously overlapped $\Delta d/d \approx 10^{-4}$.

The main advantages of EDPD over conventional powder diffraction are that the fixed detector angle makes it possible to use sample environments with windows that have only small angular openings such as a diamond anvil cell. The whole spectrum is collected simultaneously and rapidly, thus allowing the study of continuously changing phenomena such as the kinetics of phase transitions.

The main disadvantages are that the peak to peak resolution is an order of magnitude worse than the conventional powder method (making it unsuitable for studying materials of low symmetry), and the maximum count rate is limited by the detector to about 5×10^4 counts/second.

In addition the station has also been developed for Laue diffraction studies of proteins and crystal growth defects. The photon flux coming into the station is shown in fig 24, the lower energies will be severely attenuated by the Be window in the beam pipes and by air absorbtion. The spectrum seen by the specimen will therefore be more heavily weighted to the higher energies than this calculation suggests.

The new front end of station 9.7 consists of a water cooled restricting aperture to reduce the beam to a manageable size and a selection of pinholes and filters for selecting the beam size and energy distribution. Most high pressure polycrystalline diffraction is performed with a 100μm pinhole and unfiltered radiation.

Fig 25 shows an energy dispersive pattern of NBS Si 640b, the 2θ detector angle was set to 10° and the counting time was 159 seconds. The figure shows the excellent signal to raise ratio and low background that can be obtained on the new station.

Figs 26 and 27 show the energy dispersive spectra from a specimen of La_2 Cu O_4 in a diamond anvil cell mixed with NaCl at ambient pressure and 148 Kbar respectively. The detector angle was 9.8° the spectra was collected for 785s and 460s respectively. These results are displayed in figs 28 and 29 as pressure V lattice parameter. These results tie in well with recent band structure calculations [16] carried out at Daresbury Laboratory.

Fig 30 shows a spectrum taken in grazing incidence from a 50 Å layer of Cu on an Au substrate. The six peaks at lower energies are due entirely to the copper surface layer indicating that the X-ray photons are not penetrating below the surface layer until they reach an energy of 16-18 KeV. This is part of a programme to develop a method for thin film characterisation.

The structure of welded materials is of great industrial interest and is already carried out in industry by high energy X-ray and X-ray testing. An initial attempt has been made at Daresbury to map out the local structure of welded materials. Fig 31 shows an energy dispersive spectra through a 13 mm welded steel plate. The pattern took 15 minutes to collect, as expected only photons with energies larger than 60 KeV are detected. By attaching the specimen to an orientation stage and taking spectra at different angles and positions it will be possible to build up extensive information about the properties of the weld over a large region.

References

[1] B C Giessen and G E Gordon. 'X-ray Diffraction: New High-Speed Technique Based on X-ray Spectrography', Science 159, (1968), 973-975.

[2] M Mantler and W Parrish. 'Energy Dispersive X-ray Diffractormetry', Adv in X-ray Analysis, 20, (1976), 171-186.

[3] C J Sparks and D A Gedcke. 'Rapid recording of powder diffraction patterns with Si(Li) X-ray analysis system: W and Cu targets and error analysis', Adv in X-ray Analysis, 15, (1972), 240-253.

[4] B Buras, J S Olsen and L Gerward. 'White beam X-ray energy-dispersive diffractometry using synchrotron radiation', Nuclear Instruments and Methods, 152, (1978), 293-296.

[5] J Bordas, A M Glazer, C J Howard and A J Bourdillon. 'Energy-dispersive diffraction from polychrystalline materials using synchrotron radiation', Phil Mag, 35, (1977), 311-323.

[6] B Buras, 'High pressure research with synchrotron radiation', Nuclear Instruments and Methods, 208, (1983), 563-568.

[7] D R Black, C S Menoni, and Spain, I L, 'Energy-dispersive diffraction in a diamond anvil high pressure cell using synchrotron and conventional X-radiation', Adv in X-ray Anal, 27, (1984), 331-337.

[8] E S U Laine, and I T Lahteenmake, 'Order-Disorder Transformation Study in 25-35 At % Cd-Mg Alloys By Energy-Dispersive X-ray Diffraction', Mat Lett, 1, No. 5-6, (1983), 166-170.

[9] K Nisikawa, T Kazukuk and M Yositada, 'Studies of rapid structural changes in phase transitions using energy-dispersive X-ray diffractometry', in: 'X-ray Instrumentation for the Photon Factory: Dynamic Analyses of Micro Structures in Matter', ed s Hosoya, Y Iitaka, and H Hashizuma, KTK Scientific Publishers, Tokyo, (1986), 249-256.

[10] E F Skelton, A W Webb, S B Qadri, S A Wolf, R C Lacoe, J L Feldman, W T Elam, E R Carpenter Jr, and C Y Huang, 'Energy-dispersive X-ray diffraction with synchrotron radiation at cryogenic temperatures', Rev Sci Instrum, 55, No. 6, (1984), 849-855.

[11] A M Glaz er, M Hidaka and J Bordas, 'Energy-dispersive powder profile refinement using synchrotron radiation', J Appl Cryst, 11, (1978), 165-172.

[12] C N J Wager, D Lee, S Tai and I Keller, 'Energy-dispersive diffraction analysis of the structure of metallic glasses', Adv in X-ray Anal, 24, (1981), 245-252.

[13] I Takao and T Mitsuhashi, 'Energy-dispersive X-ray diffractometry for gases', in: 'X-ray Instrumentation for the Photon Factory: Dynamic Analyses of Micro Structures In Matter', ed S Hosoya, Y Iitaka and H Hashizuma, KTK Scientific Publishers, Tokyo, (1986), 257-267.

[14] P Barnes, S M Clark, S E Tarling, E Polak, D Hausermann, C Brenan, S Doyle, K J Roberts, H N Sherwood and R J Cernik, 'Synchrotron energy-dispersive powder diffraction', Daresbury Laboratory Technical Memorandum DL/SCI/TM55E, (1987).

[15] D Laundy, Private communication.

[16] M J Akhtar, C R A Catlow, S M Clark and W M Demmerman, 'The pressure dependence of the crystal structure of La_2CuO_4', Submitted to J Phys C, (1988).

Figure Captions

Fig. 1 The heating effect of the beam on the first Si(111) monochromator crystal in station 9.1. The drop in intensity of 28% after the shutter is opened can clearly be seen.

Fig. 2 This shows the spectrum obtained from Indium iodide collected at constant 2θ with the wavelength changing. The x axis shows the monochromator angle. The energy range is from 26.4 KeV at 4.3° to 9.14 KeV at 12.6°.

Fig. 3 Shows the corresponding monitor count for the energy dispersive spectrum in Fig.2.

Fig. 4 Shows the observed (upper) and calculated (lower) data for Silicalite. The calculated difference $I_{OBS}-I_{CALC}$ is shown and peak positions are also marked.

Fig. 5 Shows part of a spectrum collected on a zeolite of unknown structure.

Fig. 6 Higher angle data from the same specimens as fig. 5.

Fig. 7 Shows the raw data set collected on a Rennes standard of Barium Fluoride.

Fig. 8 Shows the 420 reflection fitted with a Pseudo-voight function.

Fig. 9 Shows the full width at half maximum height, and the integral breadths as a function of 2θ for BaF_2.

Fig. 10 Shows the same as fig. 9 for LaB_6.

Fig. 11 Shows the variation of the Gaussian β_G and Lorentzian β_L components of a Voight function fit to the peaks of LaB_6 as a function of tanθ. The sum of the component is also shown β.

Fig. 12 As fig. 11 but for BaF_2.

Fig. 13 Shows the increase in the Lorentzian fraction of the peak shape as a function of 2θ.

Fig. 14 Shows the theoretical prediction for the evaluation of an order parameter Q with time (t) together with the experimental data.

Fig. 15 Shows an expanded view of the experimental data, 1 has been annealed for 5 days, 2 for 21 days, 3 for 46 days and 4 for 64 days.

Fig. 15(a) Shows the cathodic potential deposition on a steel surface, primarily hopeite; the predicted pattern is also shown.

Fig. 15(b) Shows the result of depositions with an open potential.

Fig. 15(c) Shows the deposition under an anodic potential, the deposition is primarily phosphophyllite. The predicted structure is shown below.

Fig. 15(d) Shows the deposition of FeZn phosphate as a function of time from 0 - 300 seconds.

Fig. 16 Shows the diffractometer/furnace/position sensitive detector arrangement on station 9.1. 1 - PSD, 2 - rotating flat plate specimen holder, 3 - furnace base, 4 - beam pipe, 5 - 2θ axis.

Fig. 17 As fig. 16 but with the furnace top in position. 1 - furnace cover, 2- Be window, 3 - cooling water pipes and current leads.

Fig. 18 Shows the PSD output at 8 temperatures. 1 - 29°C, 2 - 422-427, 3 - 430-435, 4 - 437-422, 5 - 455-450, 6 - 452-457, 7 - 460 - 465, 8 - 467-472.

Fig. 18(a) Shows the 004 peak of a CdTe-InSb interface.

Fig. 18(b) Shows the 006 peak of a CdTe-InSb interface.
Interference fringes are clearly visible on both 18(a) and (b).

Fig. 19 Shows the diffractometer on station 8.3.

Fig. 20 A schematic representation of the diffractometer, showing the foils, specimen, detector and monochromator.

Fig. 21 Shows a Si 220 peak with a pseudo-Voigt fit to the observed data.

Fig. 22 Shows the raw data from the organic anti histamine agent cimetidine.

Fig. 23 Shows the calculated positions of Si diffraction lines as a function of energy and 2θ.

Fig. 24 Shows the incident flux into station 9.7.

Fig. 25 Shows an energy dispersive diffraction (EDD) pattern of Si NBS 640b.

Fig. 26 Shows the EDD pattern of La_2CuO_4 at ambient pressure.

Fig. 27 As fig. 26 but at 148 Kbar.

Fig. 28 Shows the c lattice parameter of La_2CuO_4 as a function of pressure.

Fig. 29 As fig. 28 but for c/a.

Fig. 30 Shows a grazing incidence spectrum of a 50Å layer of copper on a gold substrate

Fig. 31 Shows an EDD spectrum through a 13 nm welded steel plate.

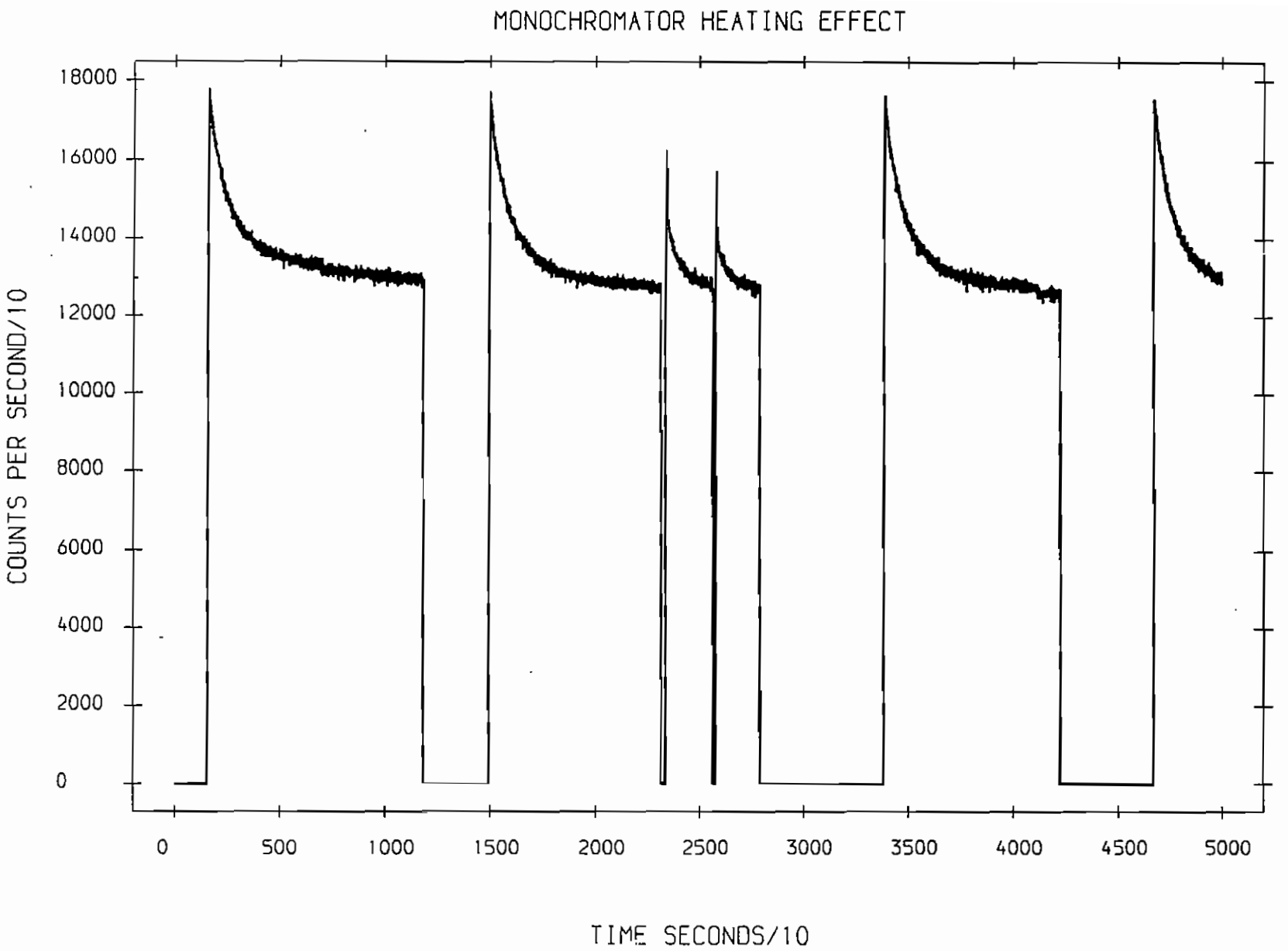
MONOCHROMATOR HEATING EFFECT
COUNTS PER SECOND/10
18000
16000
14000
12000
10000
8000
6000
4000
2000
0
0
500
1000
1500
2000
2500
3000
3500
4000
4500
5000
TIME SECONDS/10

Fig.1

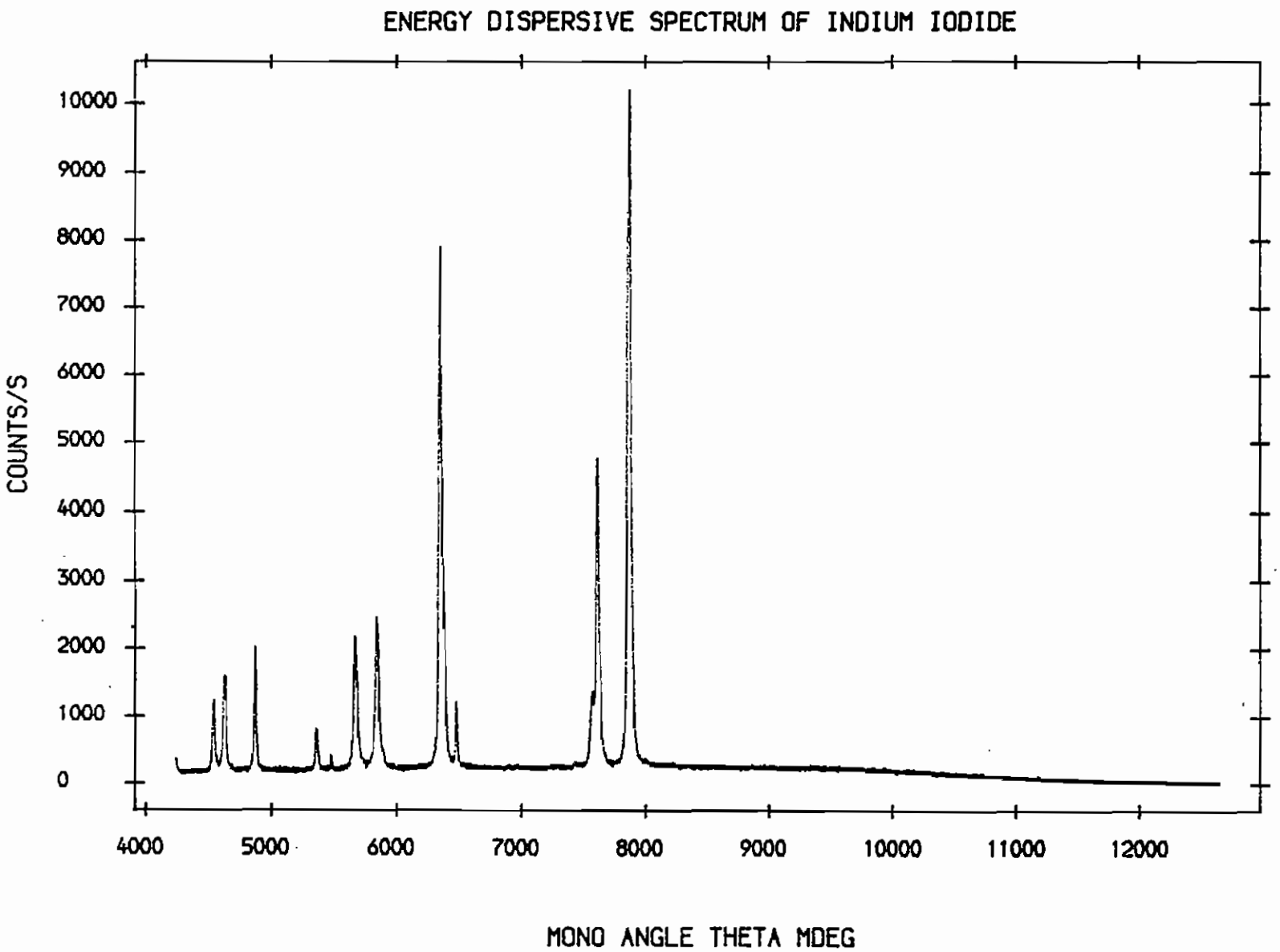
ENERGY DISPERSIVE SPECTRUM OF INDIUM IODIDE
COUNTS/S
10000
9000
8000
7000
6000
5000
4000
3000
2000
1000
0
4000
5000
6000
7000
8000
9000
10000
11000
12000
MONO ANGLE THETA MDEG

Fig.2

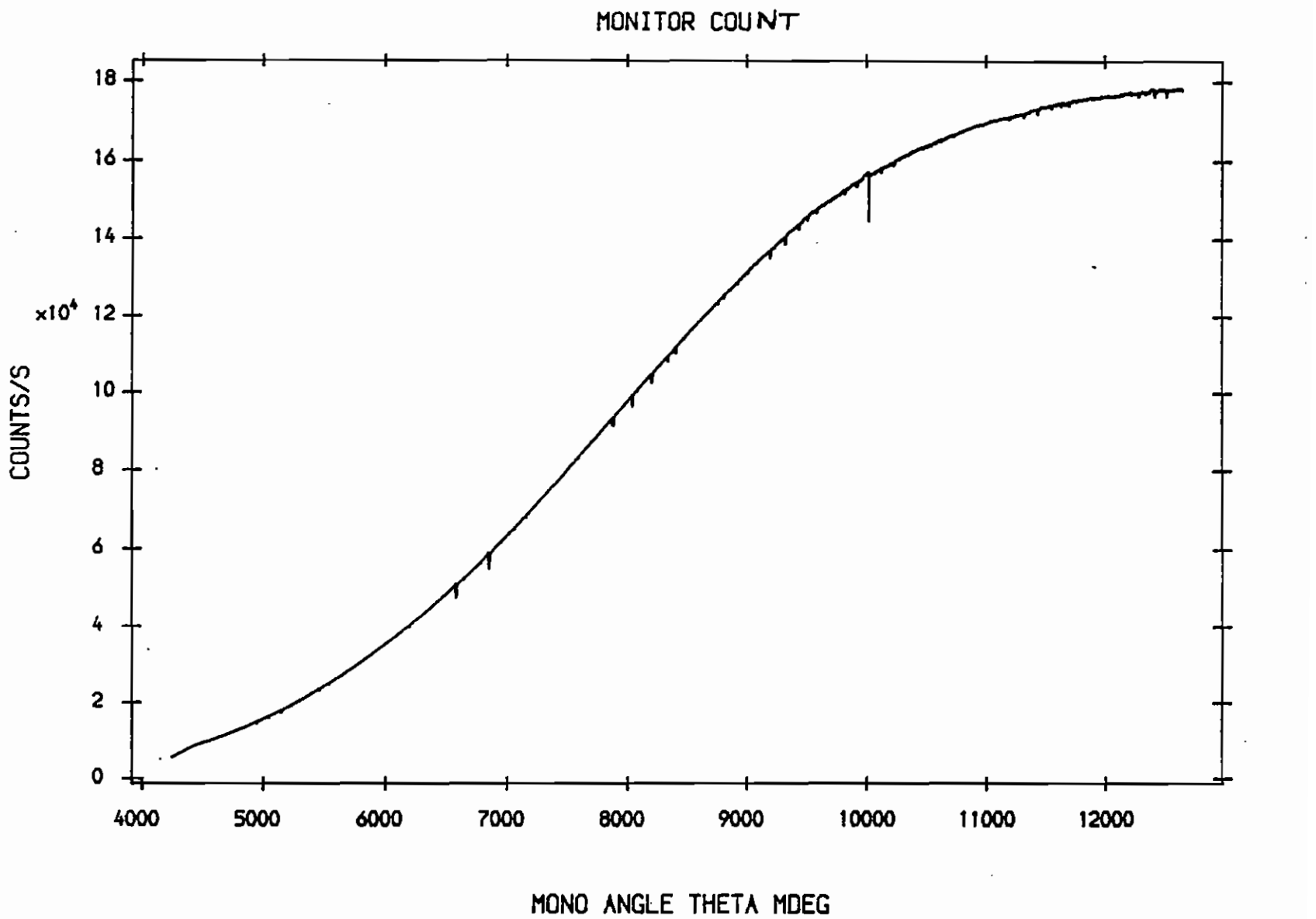
MONITOR COUNT
COUNTS/S
x10⁴
18
16
14
12
10
8
6
4
2
0
4000
5000
6000
7000
8000
9000
10000
11000
12000
MONO ANGLE THETA MDEG

Fig.3

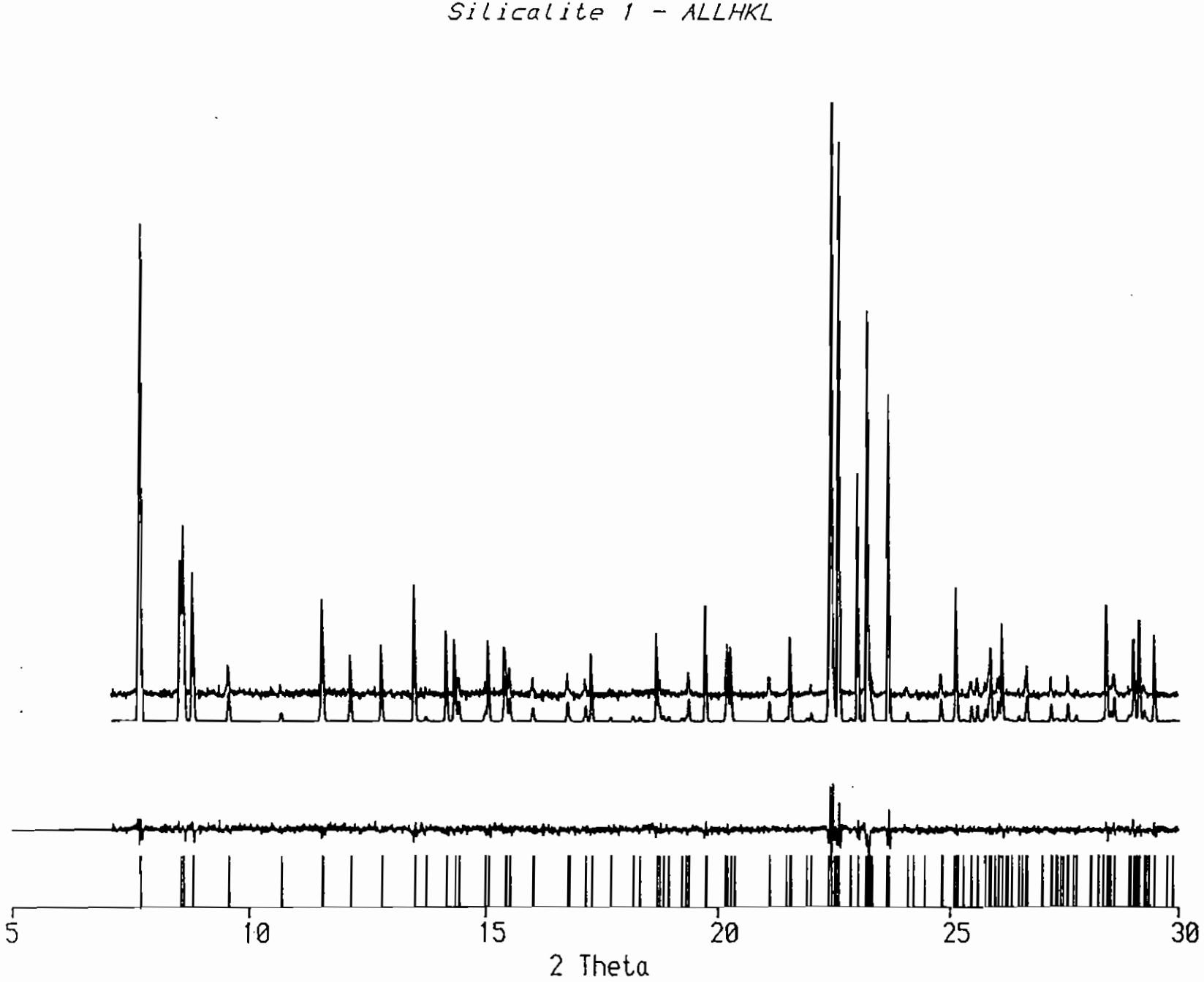

Fig.4

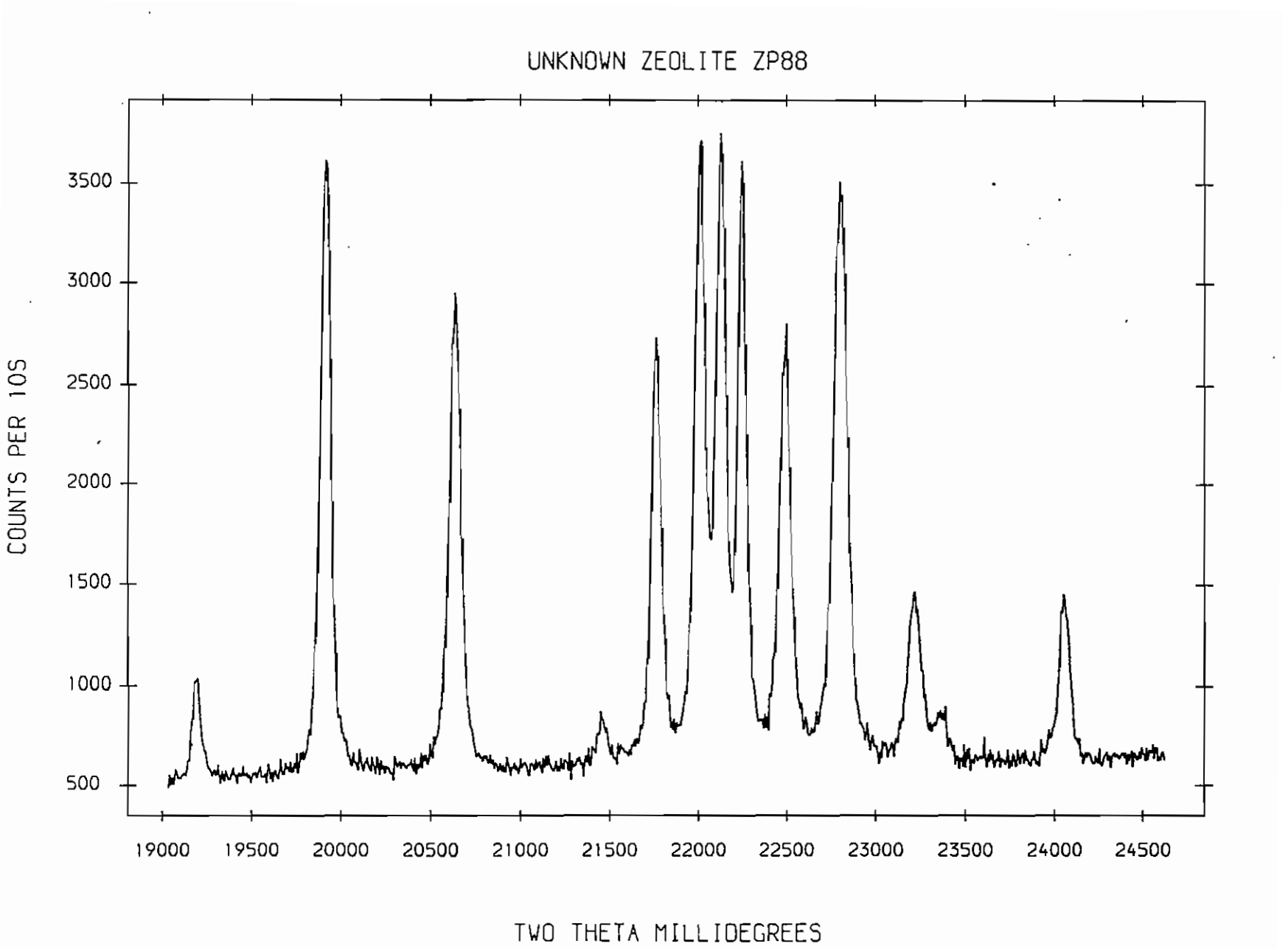
UNKNOWN ZEOLITE ZP88
COUNTS PER 10S
3500
3000
2500
2000
1500
1000
500
19000
19500
20000
20500
21000
21500
22000
22500
23000
23500
24000
24500
TWO THETA MILLIDEGREES

Fig.5

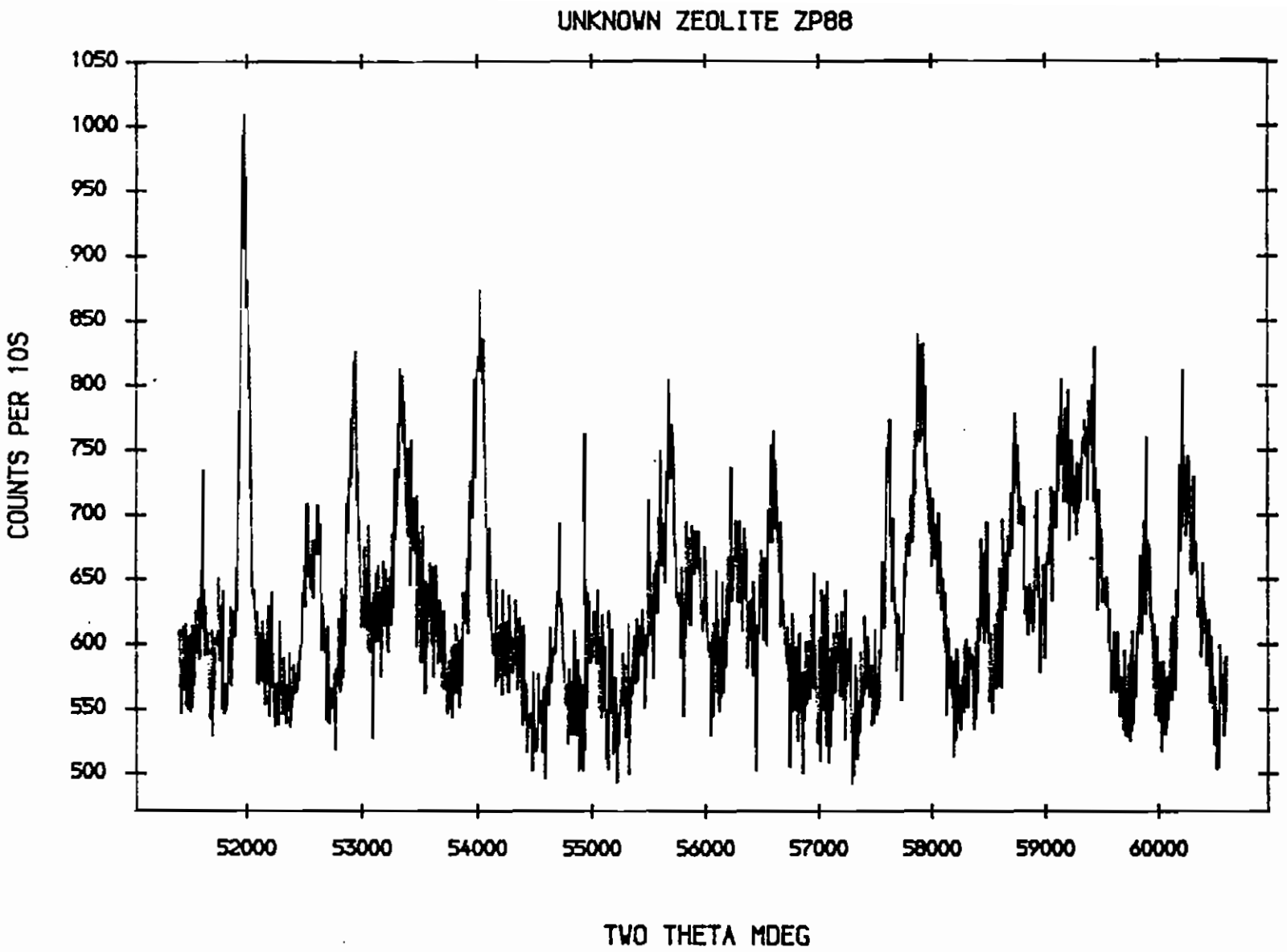
UNKNOWN ZEOLITE ZP88
COUNTS PER 10S
1050
1000
950
900
850
800
750
700
650
600
550
500
52000
53000
54000
55000
56000
57000
58000
59000
60000
TWO THETA MDEG

Fig.6

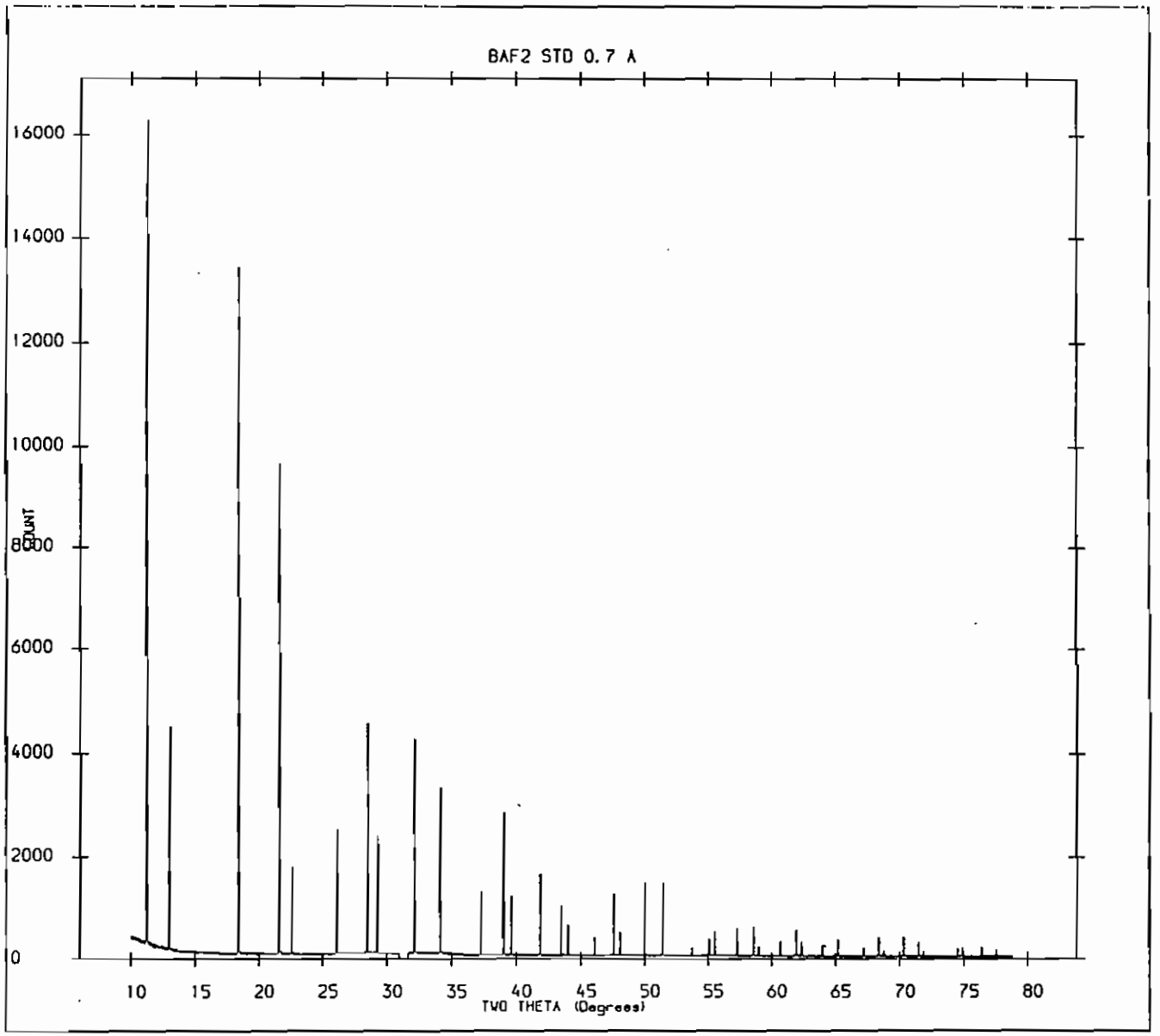
BAF2 STD 0.7 A
16000
14000
12000
10000
8000
6000
4000
2000
0
COUNT
10
15
20
25
30
35
40
45
50
55
60
65
70
75
80
TWO THETA (Degrees)

Fig.7

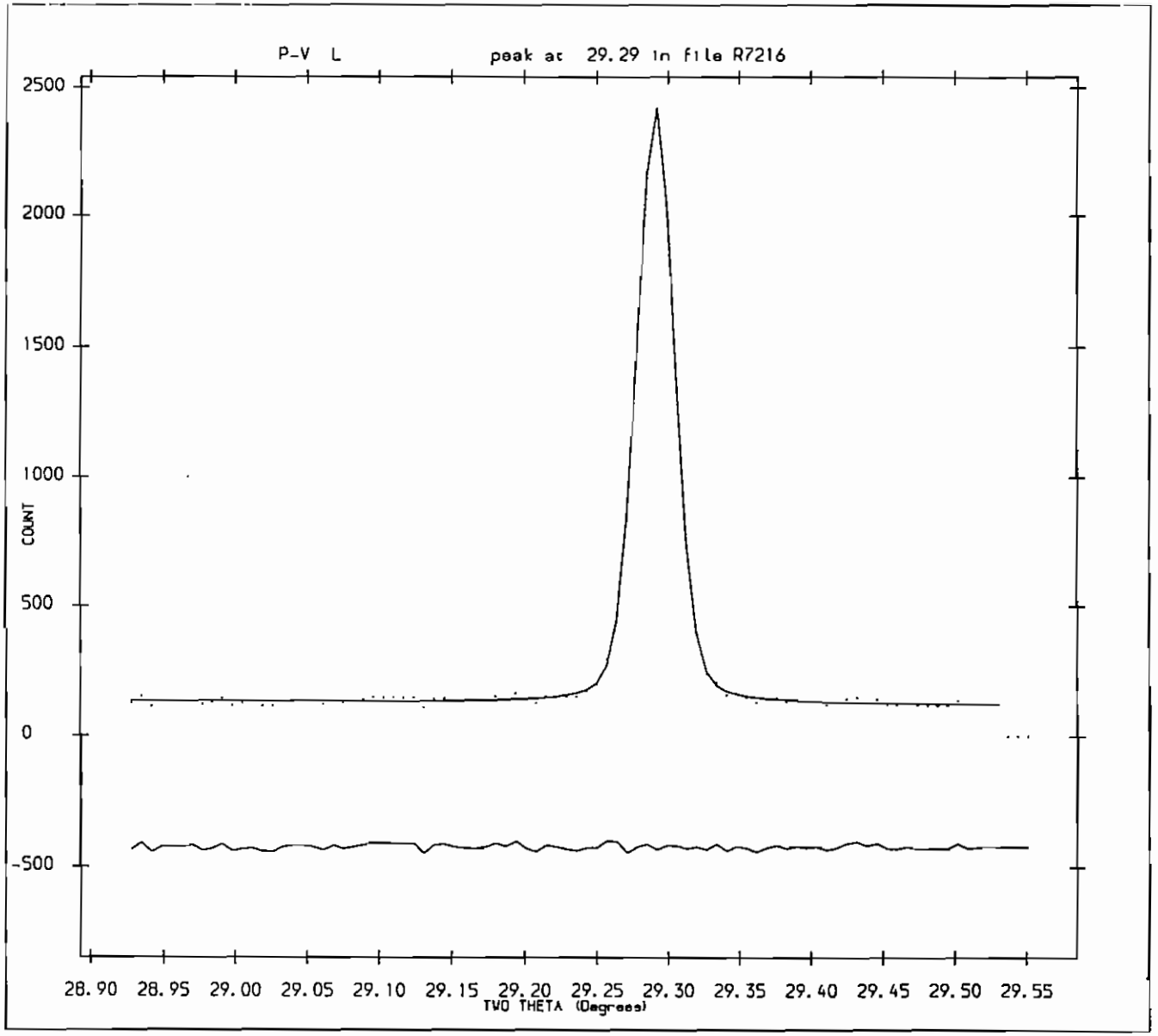
P-V L
peak at 29.29 in file R7216
2500
2000
1500
1000
500
0
-500
COUNT
28.90
28.95
29.00
29.05
29.10
29.15
29.20
29.25
29.30
29.35
29.40
29.45
29.50
29.55
TWO THETA (Degrees)

Fig.8

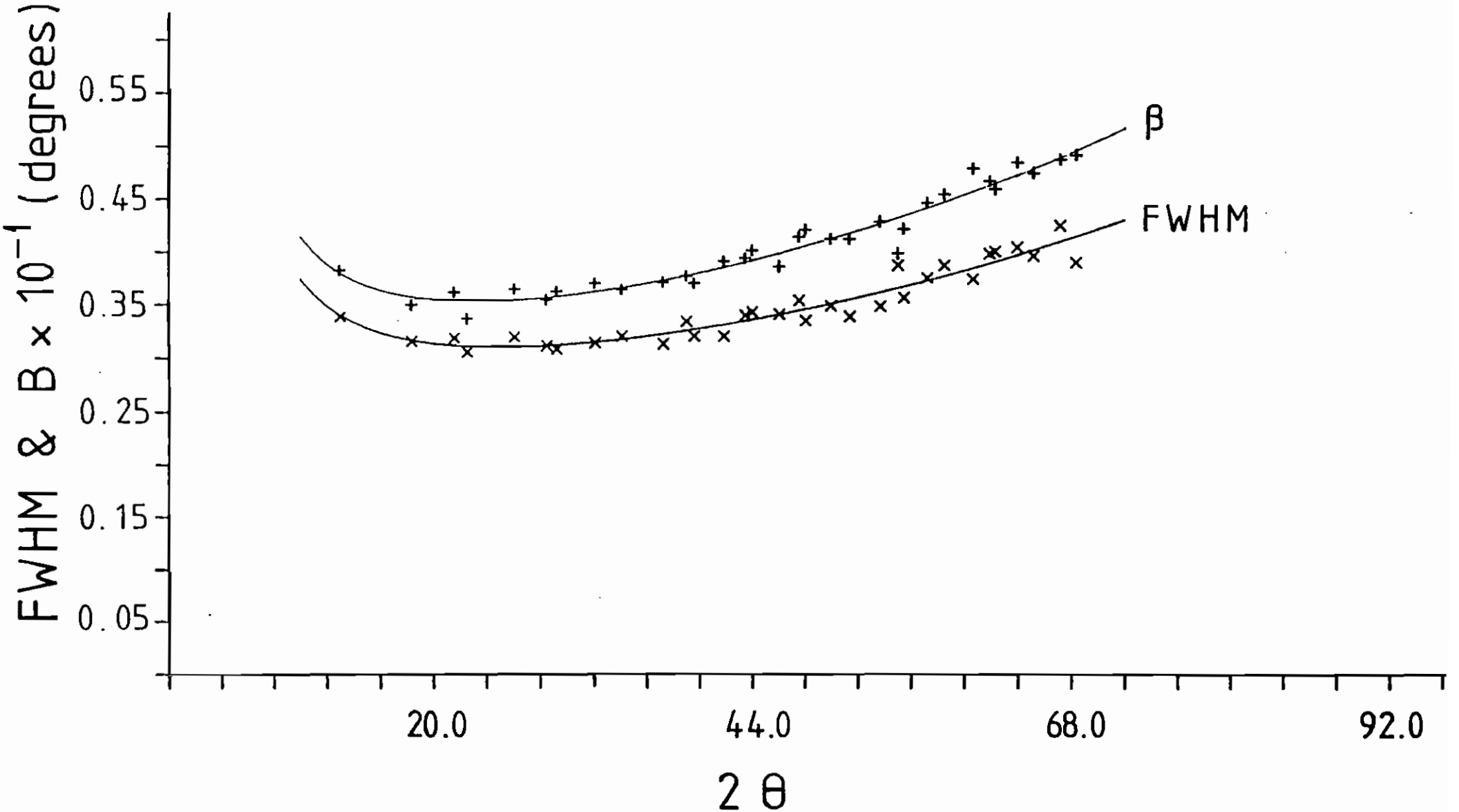
FWHM & B x 10⁻¹ (degrees)
0.55
0.45
0.35
0.25
0.15
0.05
β
FWHM
20.0
44.0
68.0
92.0
2 θ

Fig.9

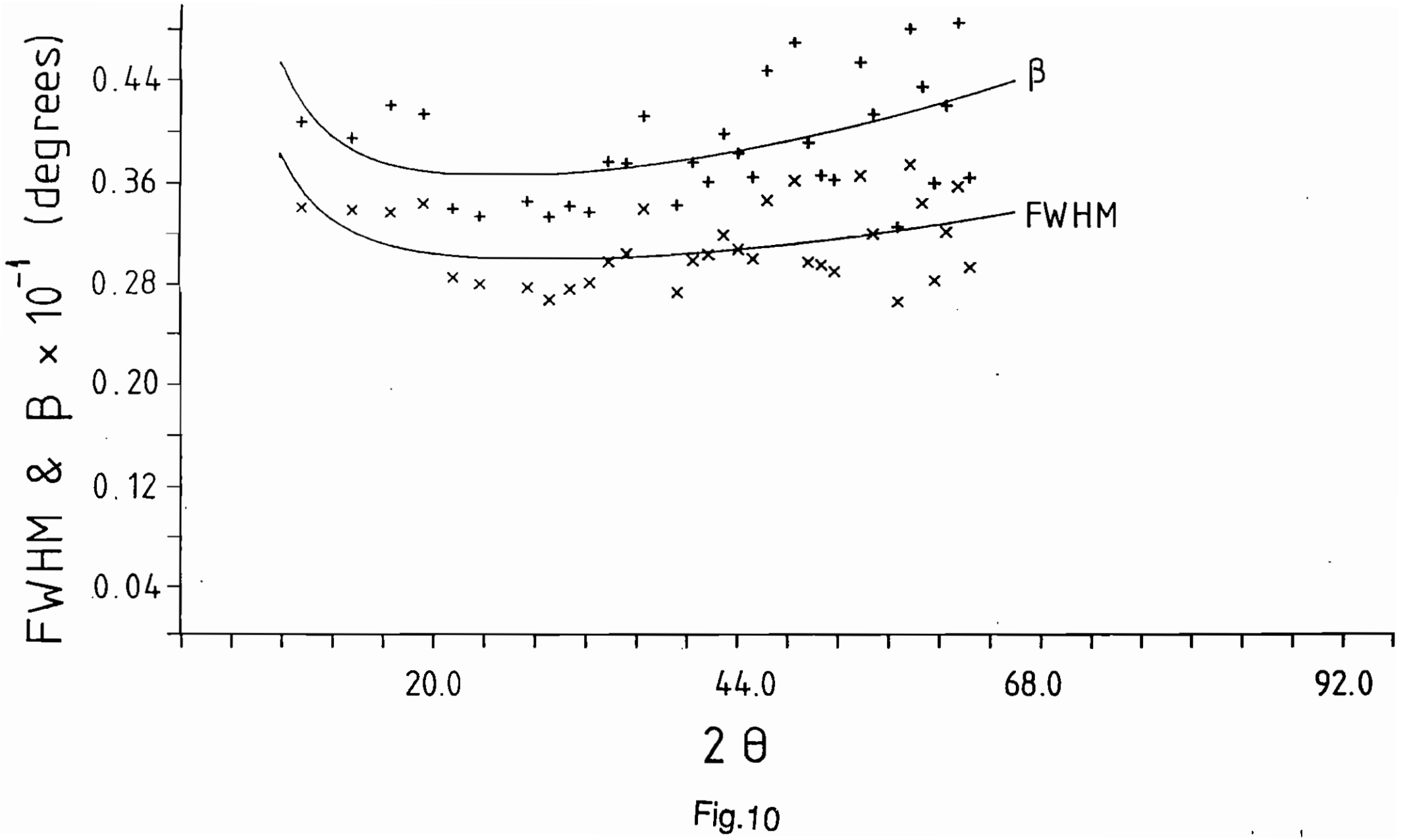
FWHM & β x 10⁻¹ (degrees)
0.44
0.36
0.28
0.20
0.12
0.04
β
FWHM
20.0
44.0
68.0
92.0
2 θ

Fig.10

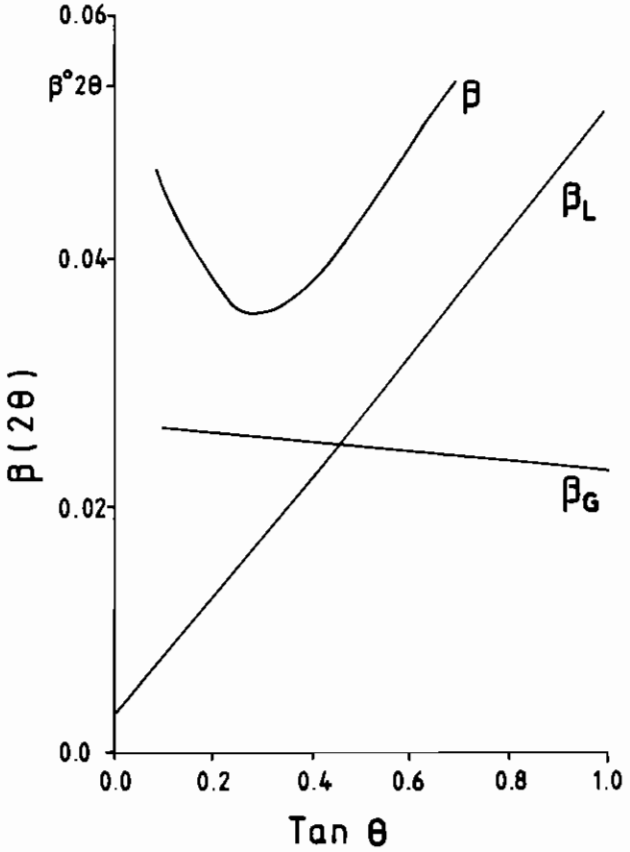

FIG. 11

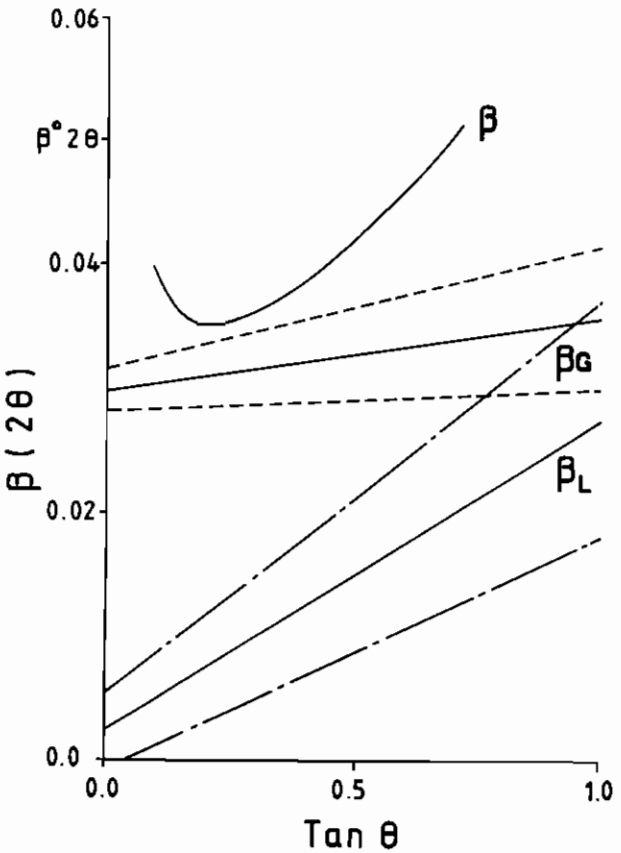

FIG. 12

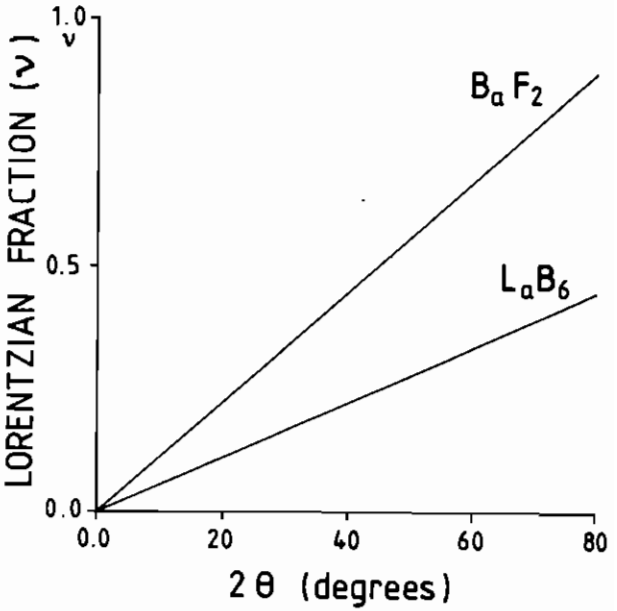

FIG. 13

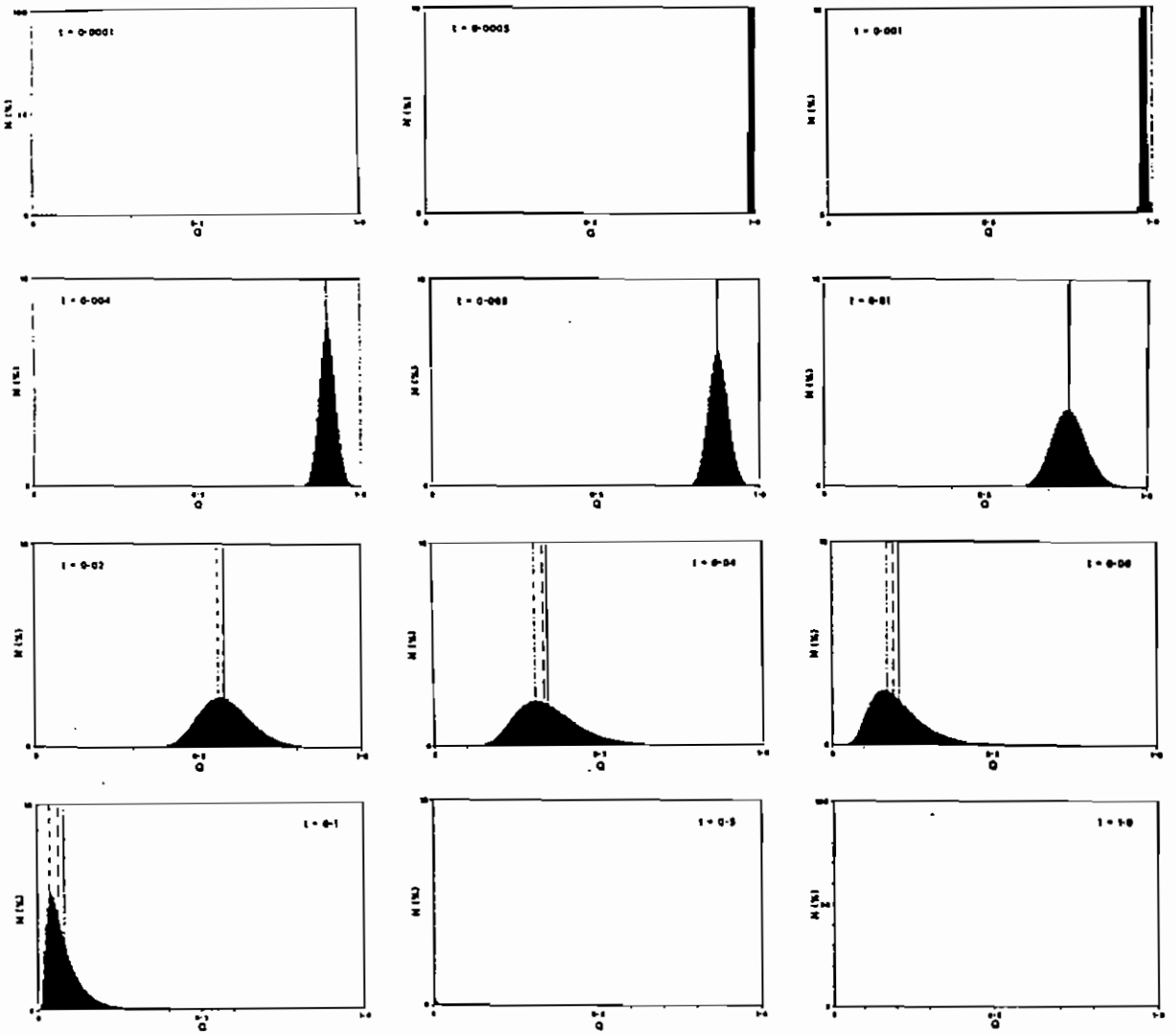

a) Theoretical prediction of evolution of order parameter (Q) with time (t)

Fig.14(a)

Time evolution of the 131 peak in annealed Albite samples.

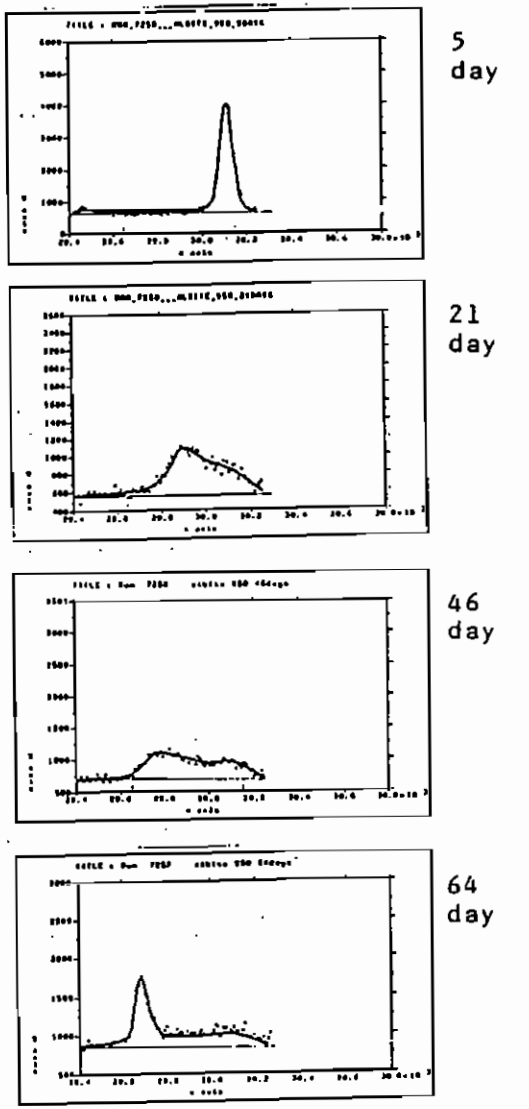

b) Experimental observation

Fig.14(b)

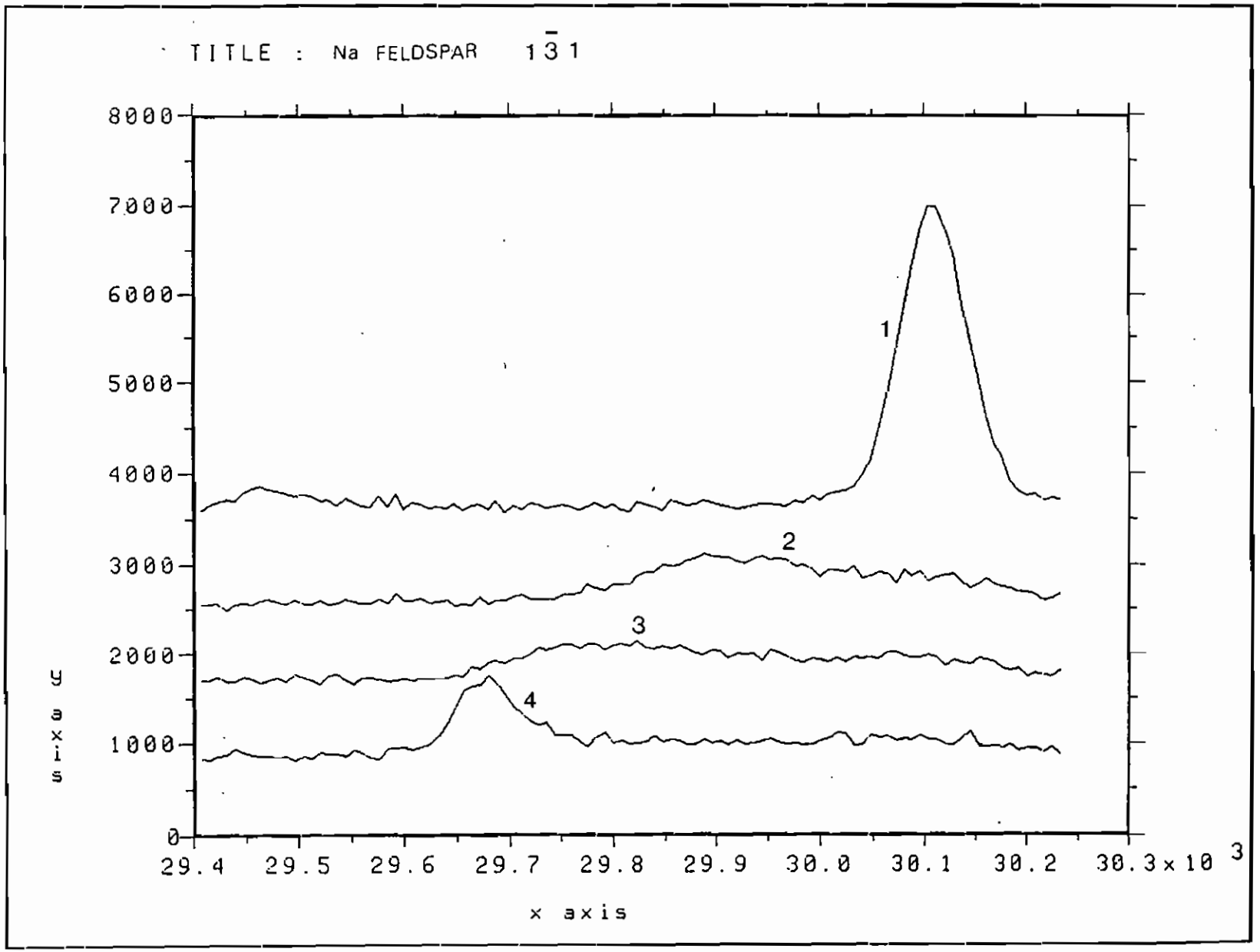
TITLE : Na FELDSPAR 1 3̄ 1
8000
7000
6000
5000
4000
3000
2000
1000
0
y axis
1
2
3
4
29.4
29.5
29.6
29.7
29.8
29.9
30.0
30.1
30.2
30.3 x 10 3
x axis

Fig.15

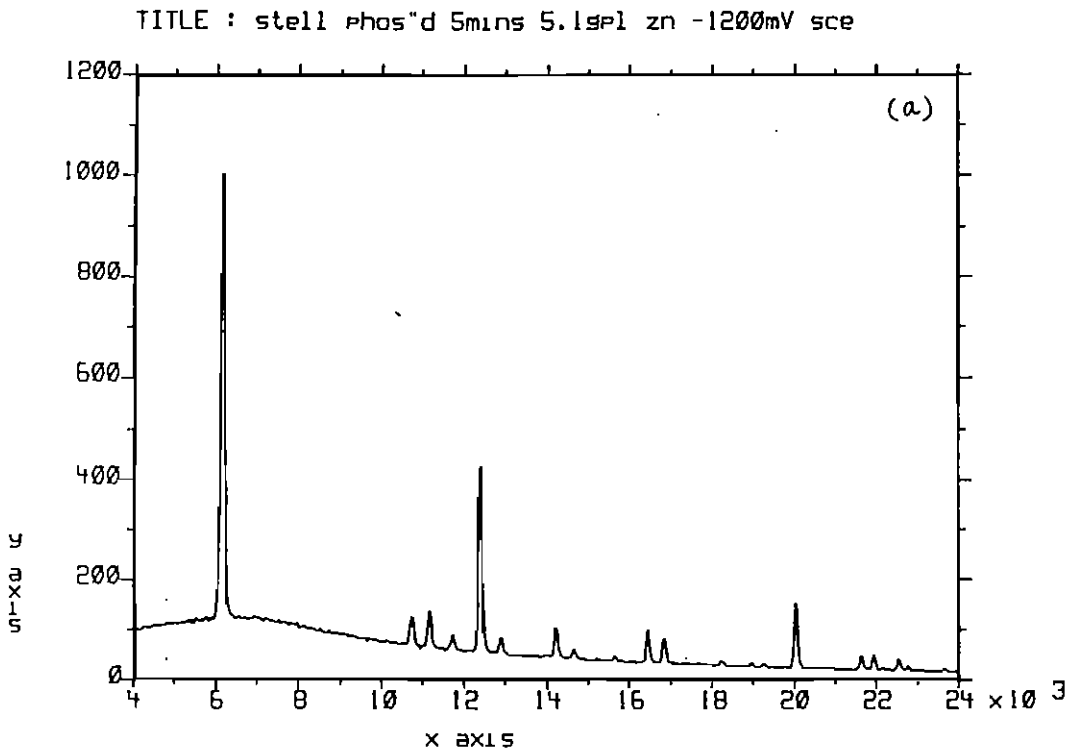
TITLE : stell phos"d 5mins 5.1gpl zn -1200mV sce
(a)
1200
1000
800
600
400
200
0
4
6
8
10
12
14
16
18
20
22
24
x10 3
x axis
y axis

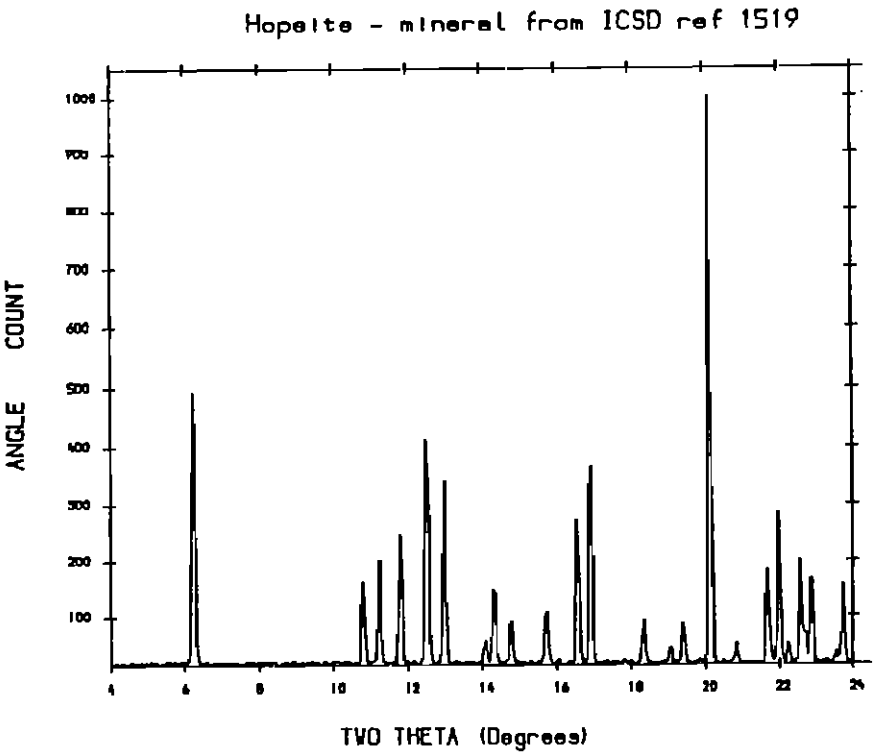
Hopeite - mineral from ICSD ref 1519
ANGLE COUNT
TWO THETA (Degrees)

Fig.15(a)

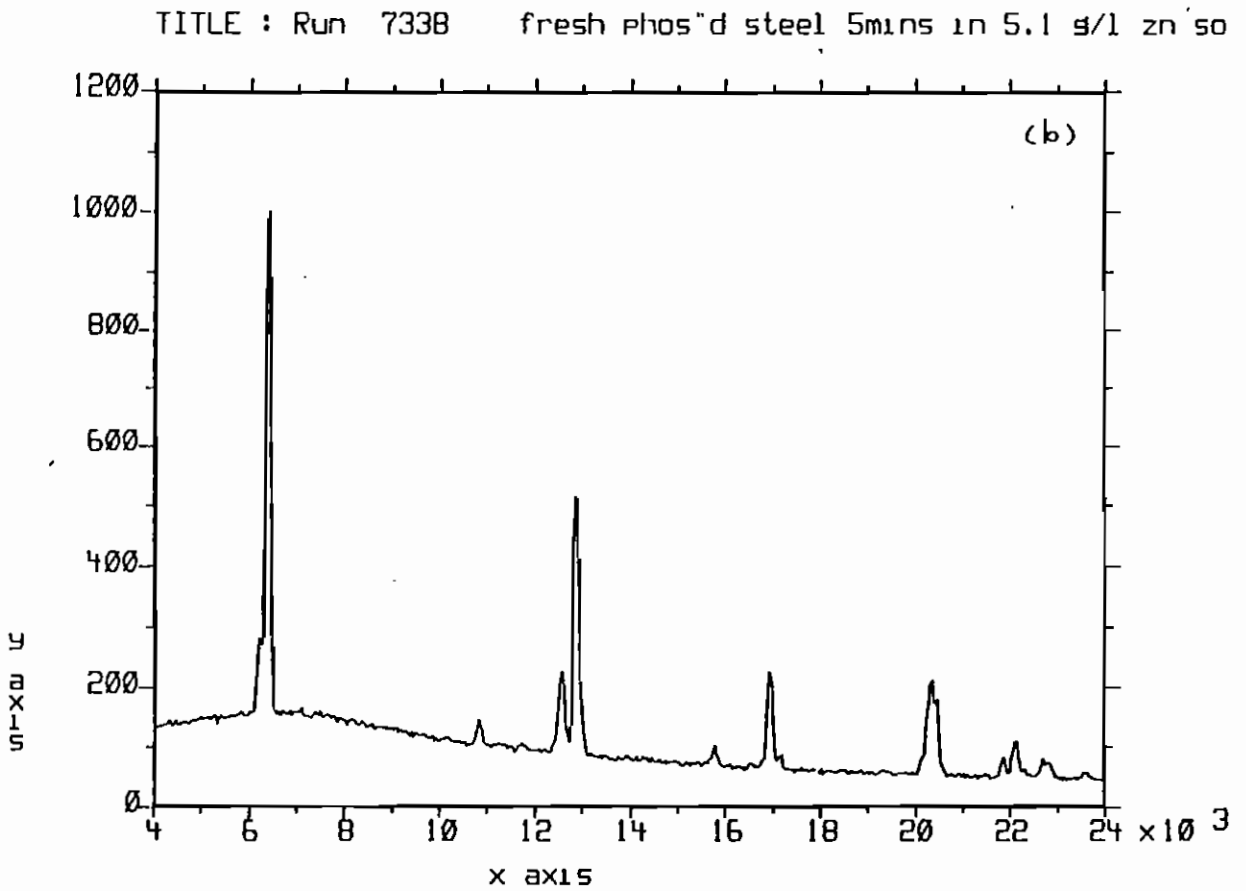
TITLE : Run 7338 fresh phos"d steel 5mins in 5.1 g/l zn so
(b)
1200
1000
800
600
400
200
0
y axis
4
6
8
10
12
14
16
18
20
22
24
x10 3
x axis

Fig.15(b)

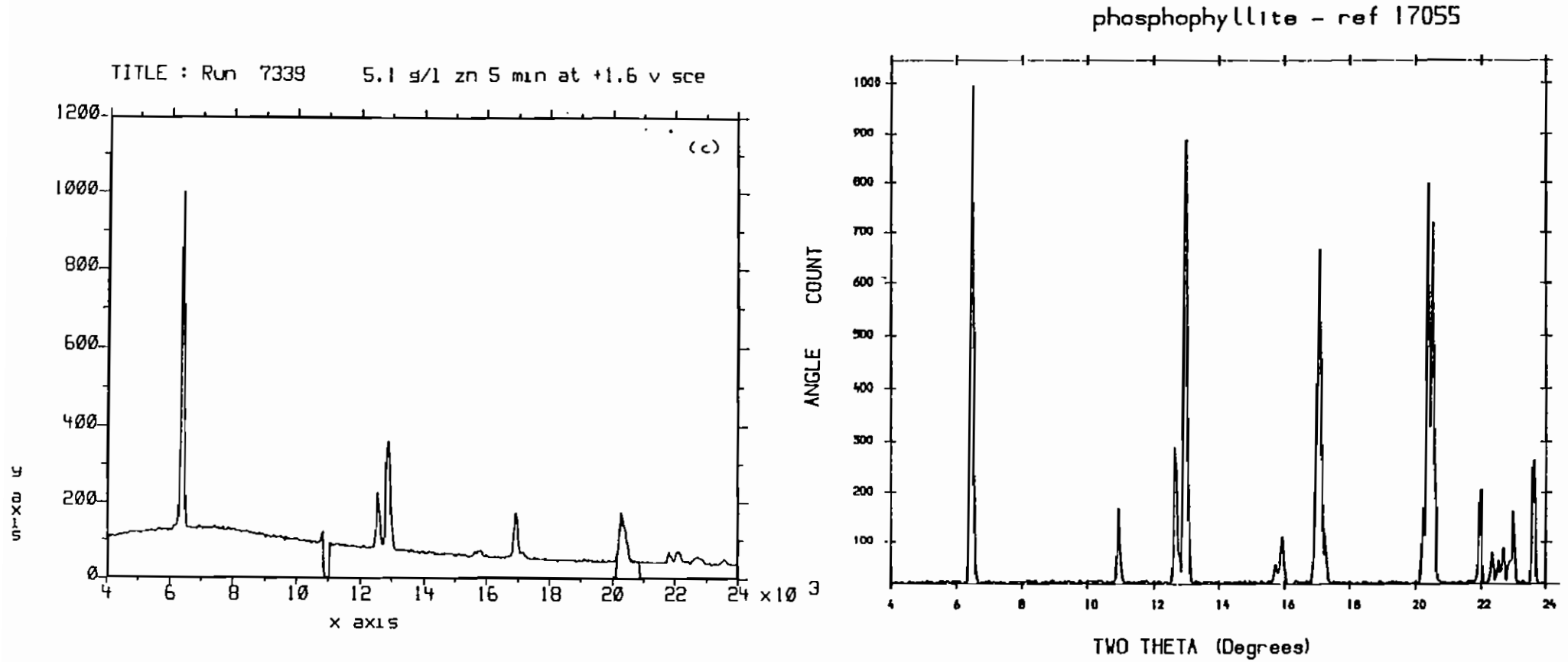
TITLE : Run 7339 5.1 g/l zn 5 min at +1.6 v sce
(c)
1200
1000
800
600
400
200
0
4
6
8
10
12
14
16
18
20
22
24
x10 3
x axis
y axis
phosphophyllite - ref 17055
ANGLE COUNT
TWO THETA (Degrees)

Fig.15(c)

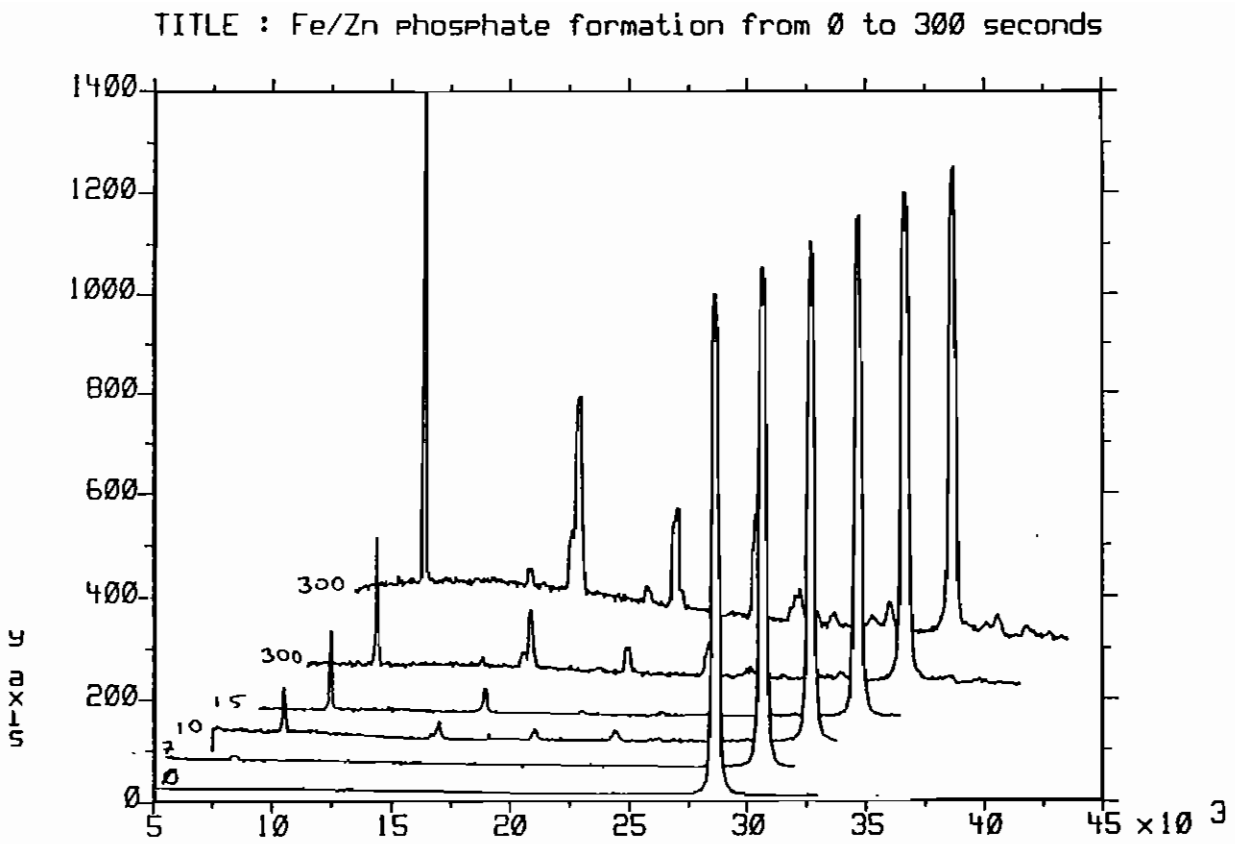
TITLE : Fe/Zn phosphate formation from 0 to 300 seconds
1400
1200
1000
800
600
400
200
0
counts
300
300
15
10
2
0
5
10
15
20
25
30
35
40
45 x10 3

Fig.15(d)

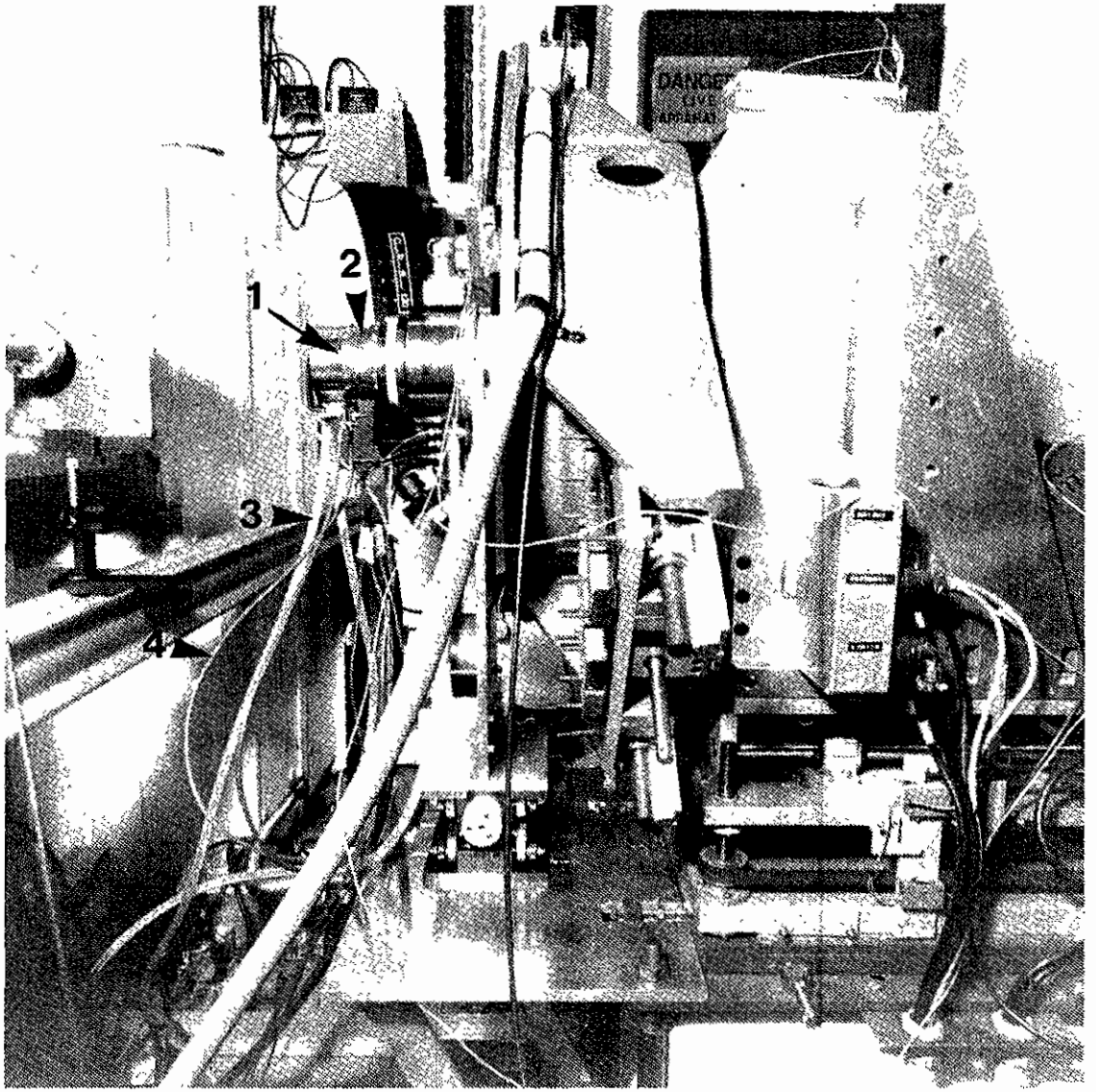

Fig. 16

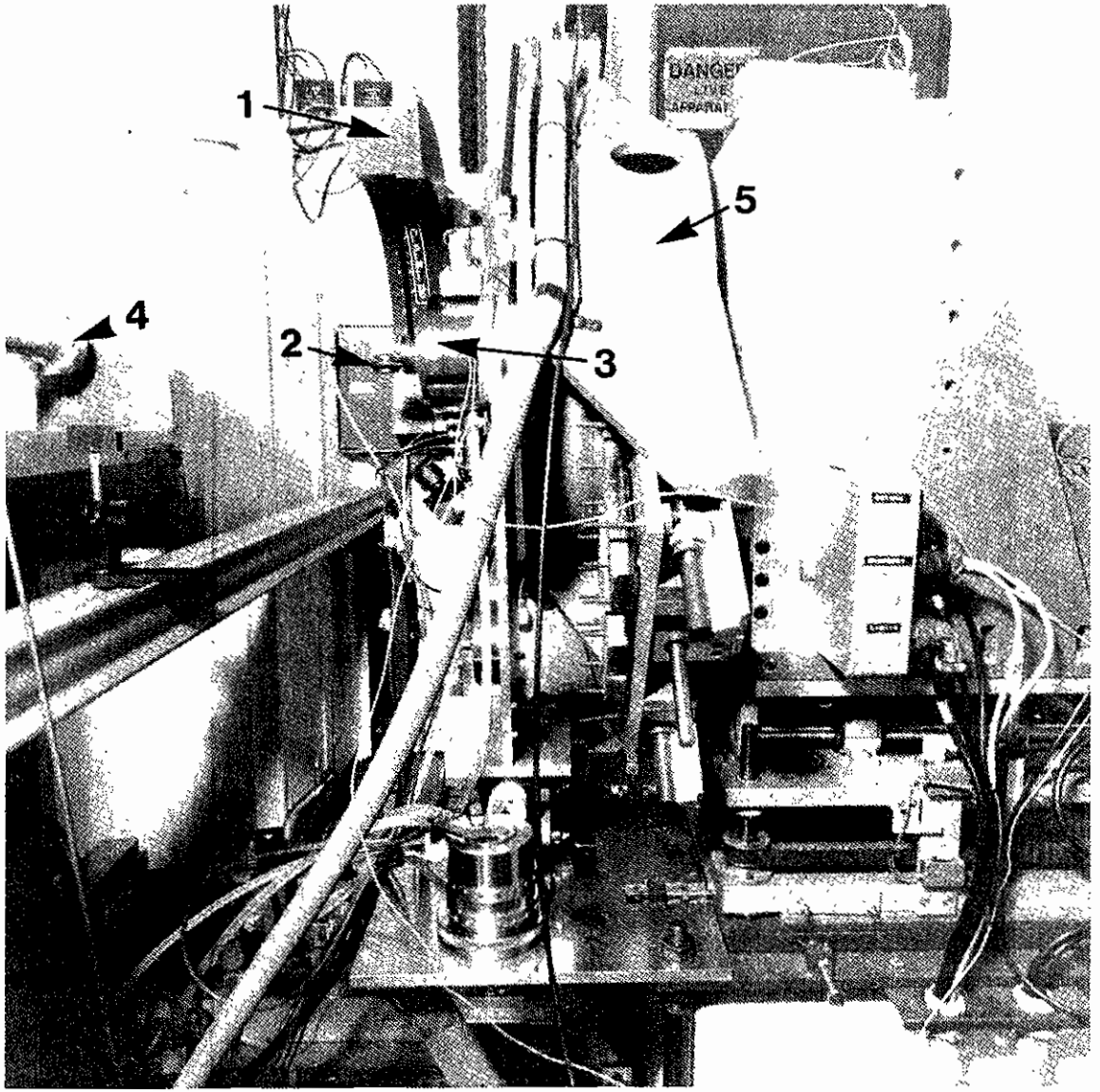

Fig. 17

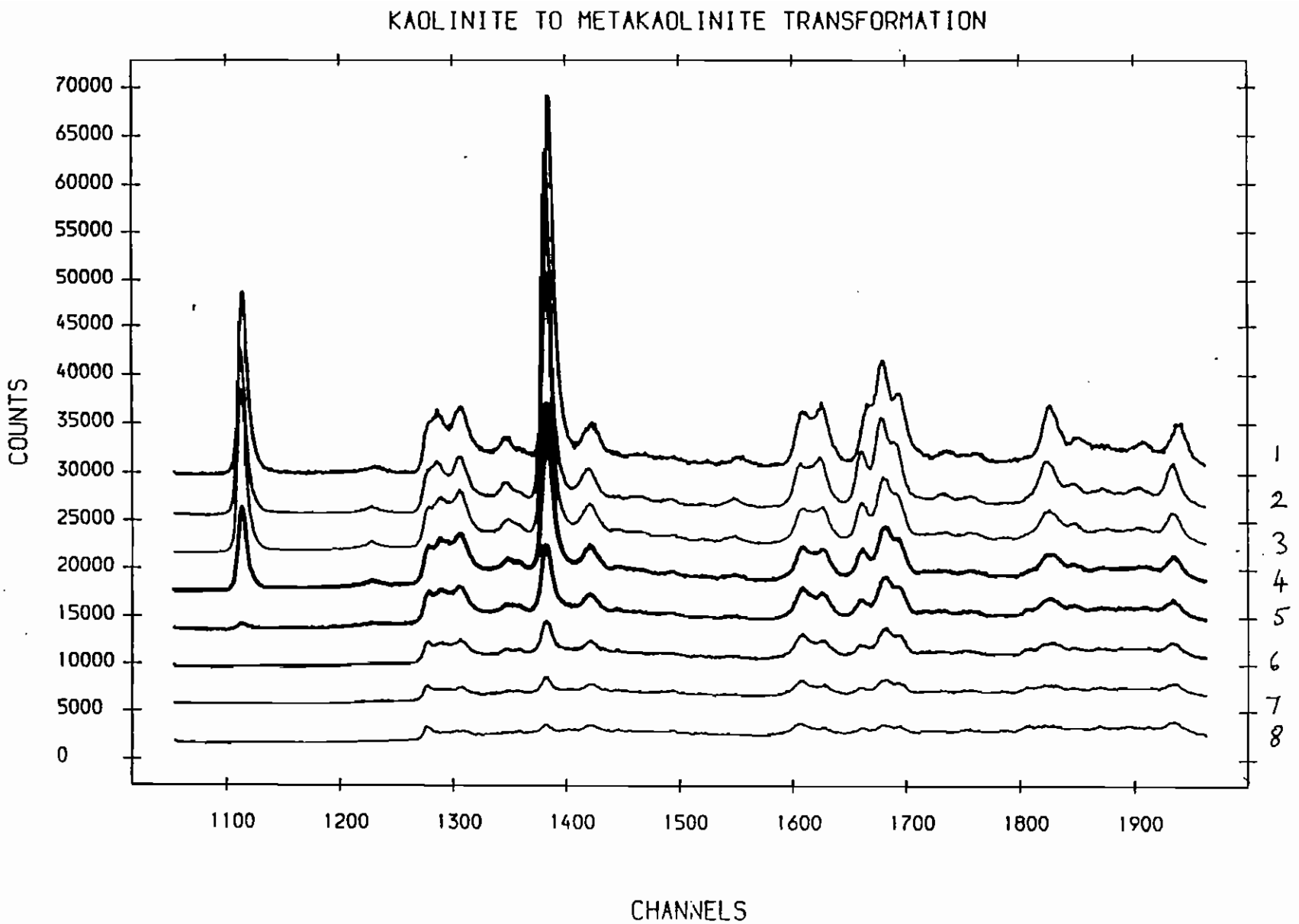
KAOLINITE TO METAKAOLINITE TRANSFORMATION
COUNTS
70000
65000
60000
55000
50000
45000
40000
35000
30000
25000
20000
15000
10000
5000
0
1100
1200
1300
1400
1500
1600
1700
1800
1900
CHANNELS
1
2
3
4
5
6
7
8

Fig.18

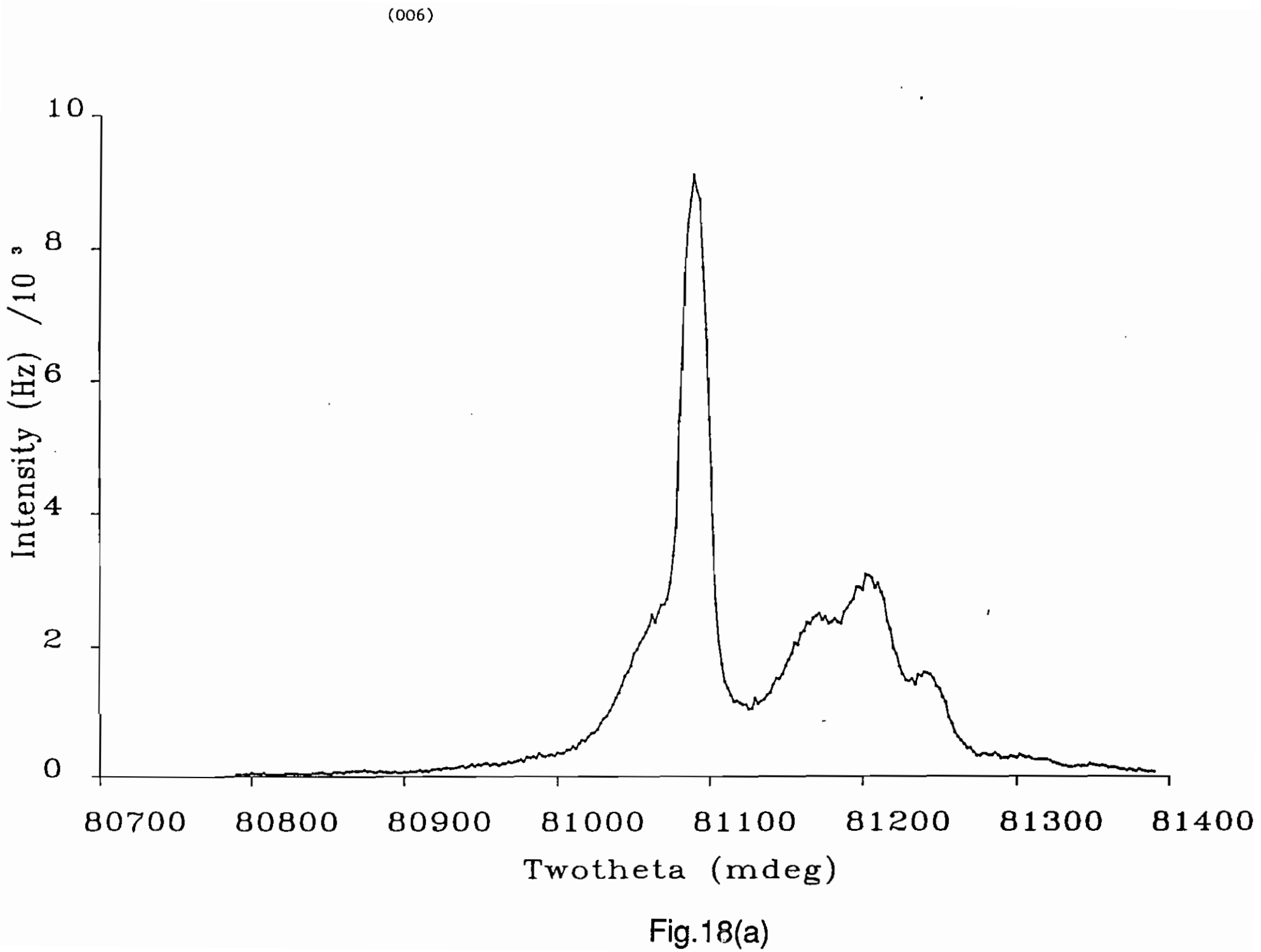
(006)
10
8
6
4
2
0
Intensity (Hz) /10 ³
80700
80800
80900
81000
81100
81200
81300
81400
Twotheta (mdeg)

Fig.18(a)

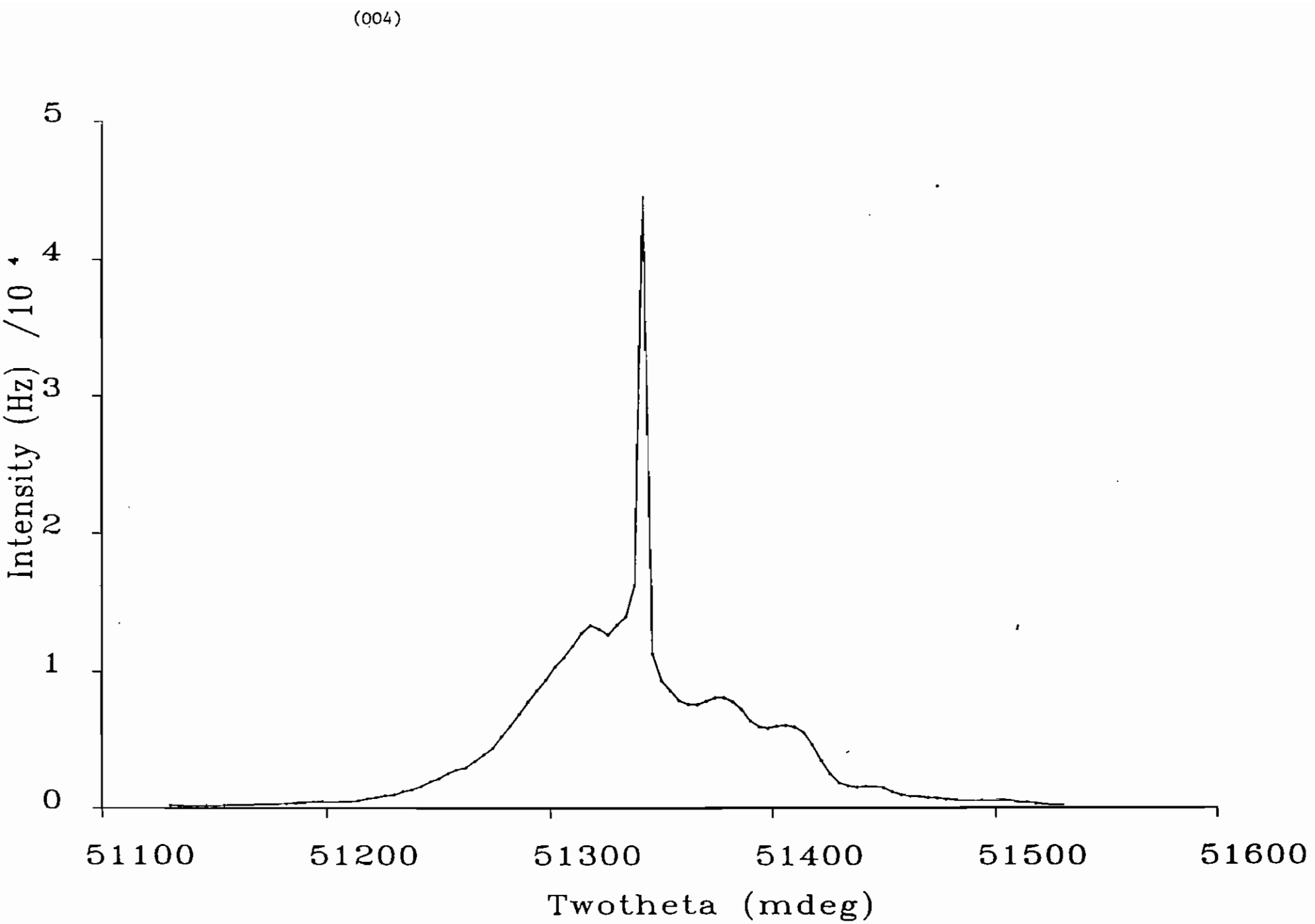
(004)
5
4
3
2
1
0
Intensity (Hz) /10 4
51100
51200
51300
51400
51500
51600
Twotheta (mdeg)

Fig.18(b)

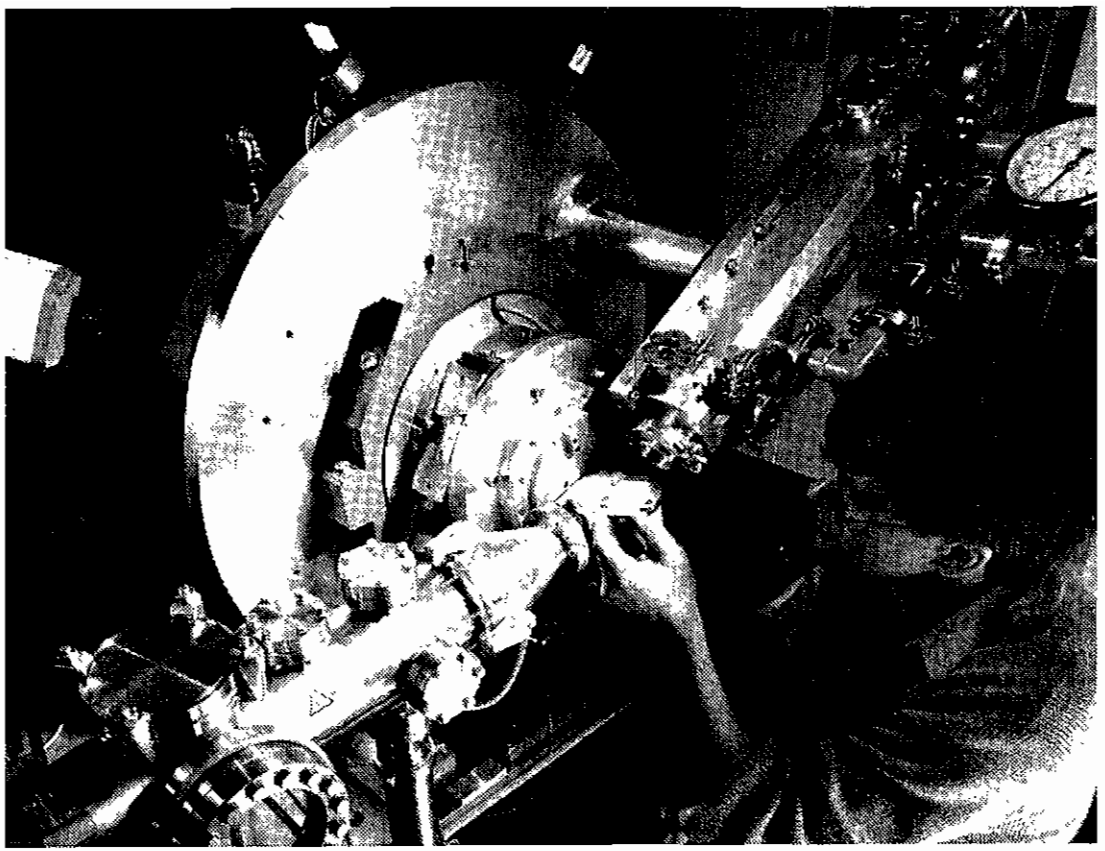

Fig. 19

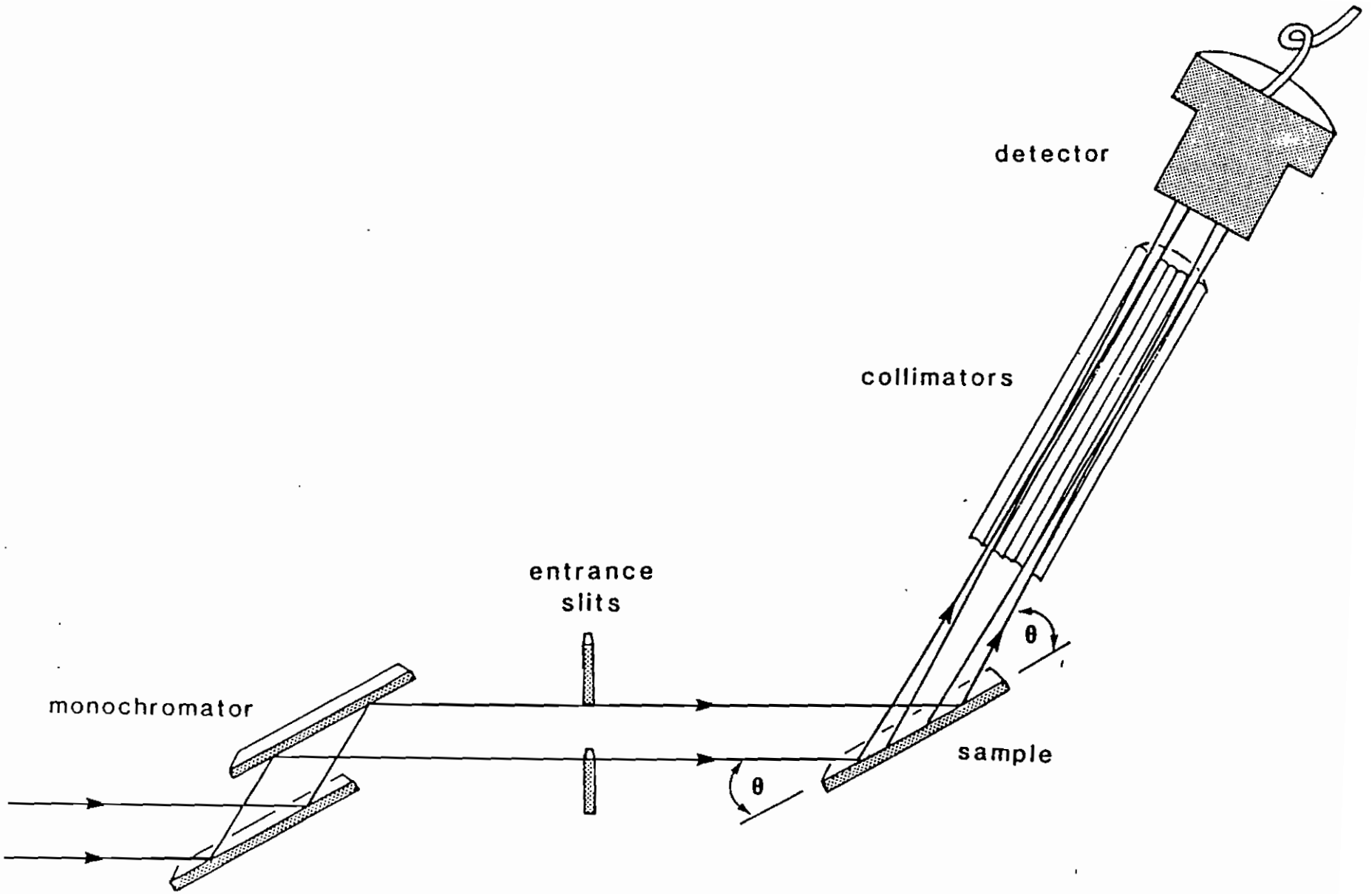
detector
collimators
entrance
slits
θ
monochromator
sample
θ

Fig.20

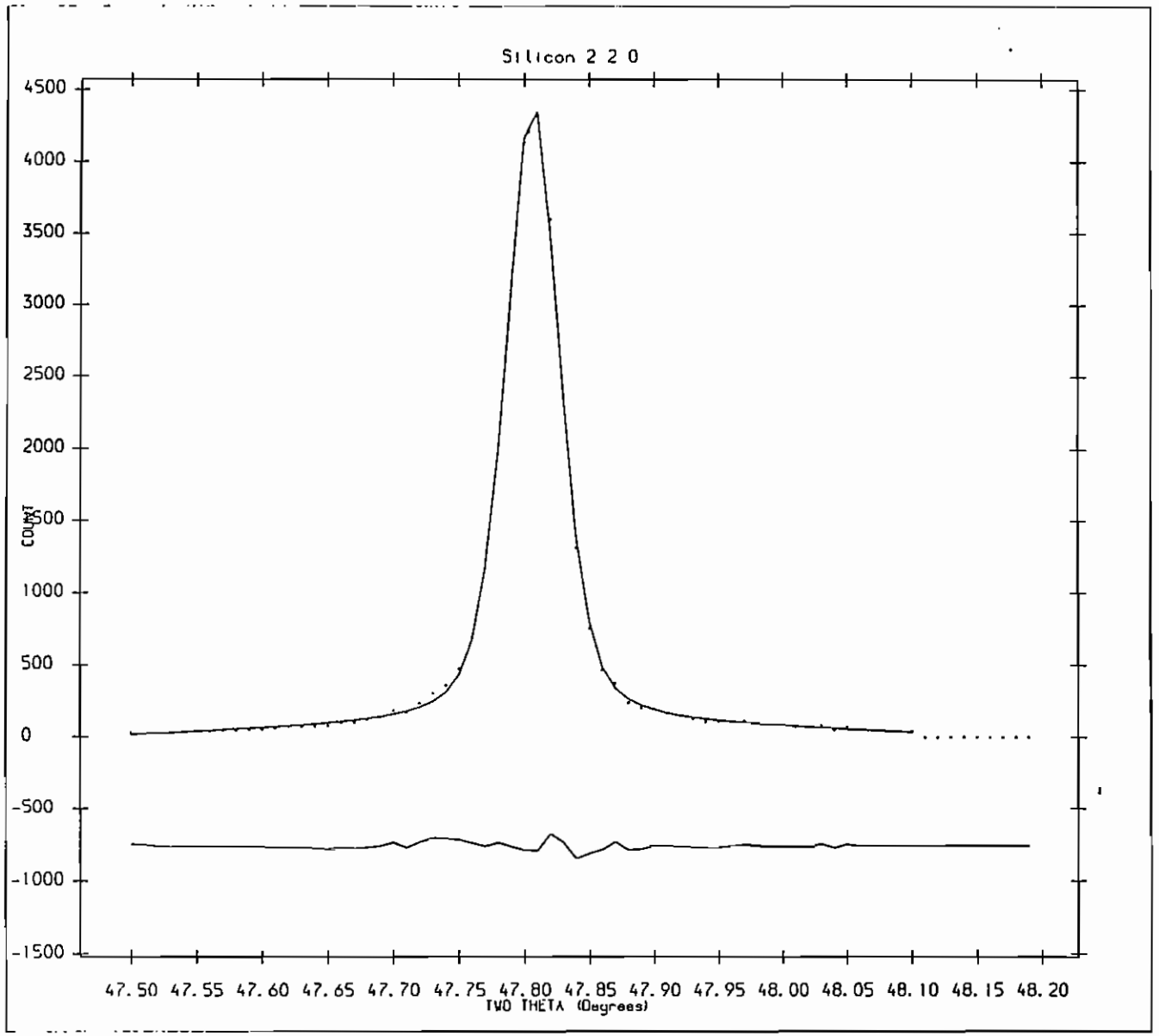
Silicon 2 2 0
4500
4000
3500
3000
2500
2000
1500
1000
500
0
-500
-1000
-1500
COUNTS
47.50 47.55 47.60 47.65 47.70 47.75 47.80 47.85 47.90 47.95 48.00 48.05 48.10 48.15 48.20
TWO THETA (Degrees)

Fig.21

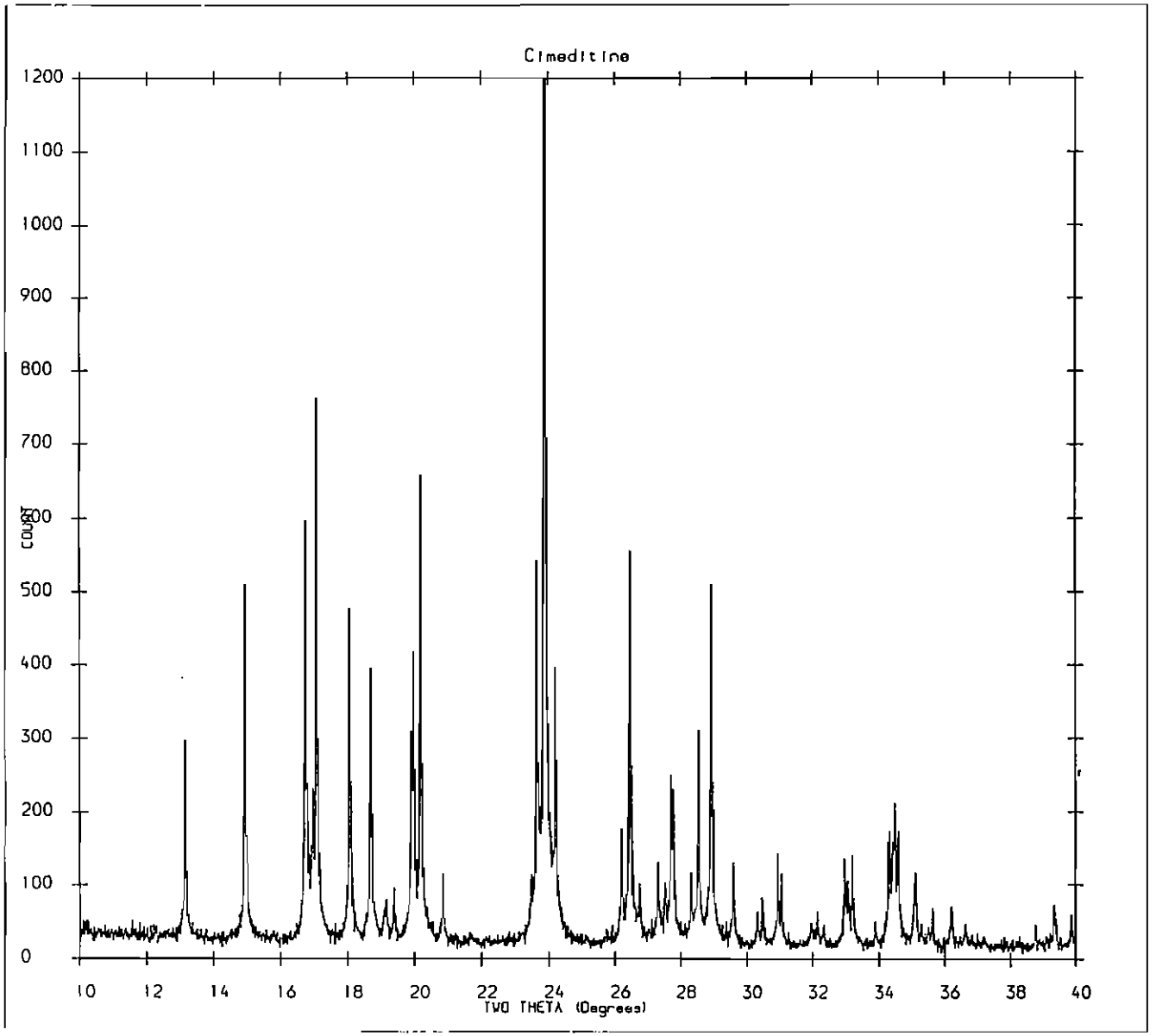
Cimeditine
1200
1100
1000
900
800
700
600
500
400
300
200
100
0
COUNT
10
12
14
16
18
20
22
24
26
28
30
32
34
36
38
40
TWO THETA (Degrees)

Fig.22

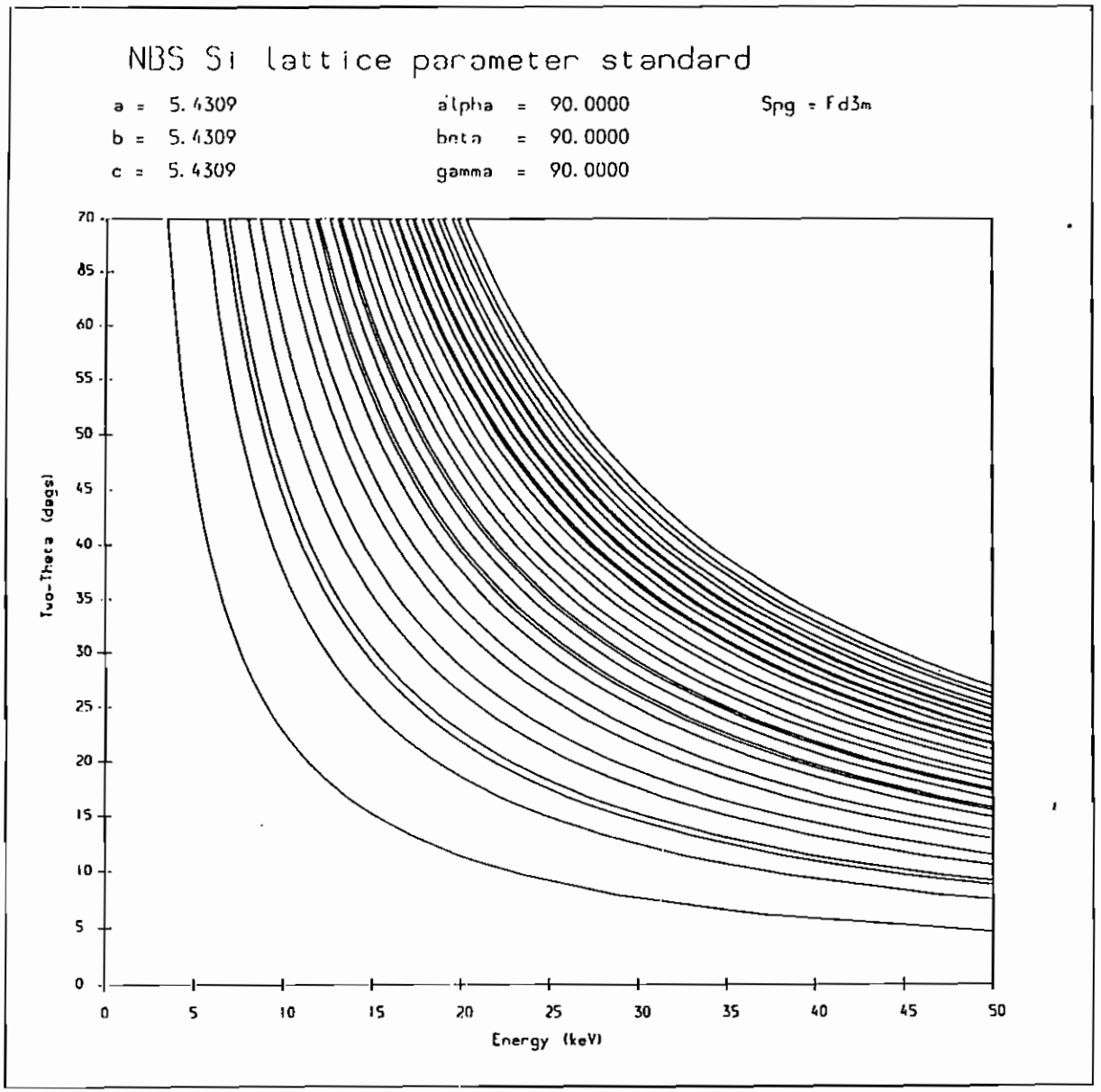
NBS Si lattice parameter standard
a = 5.4309
b = 5.4309
c = 5.4309
alpha = 90.0000
beta = 90.0000
gamma = 90.0000
Spg = Fd3m
Two-Theta (degs)
Energy (keV)
0
5
10
15
20
25
30
35
40
45
50
55
60
65
70

Fig.23

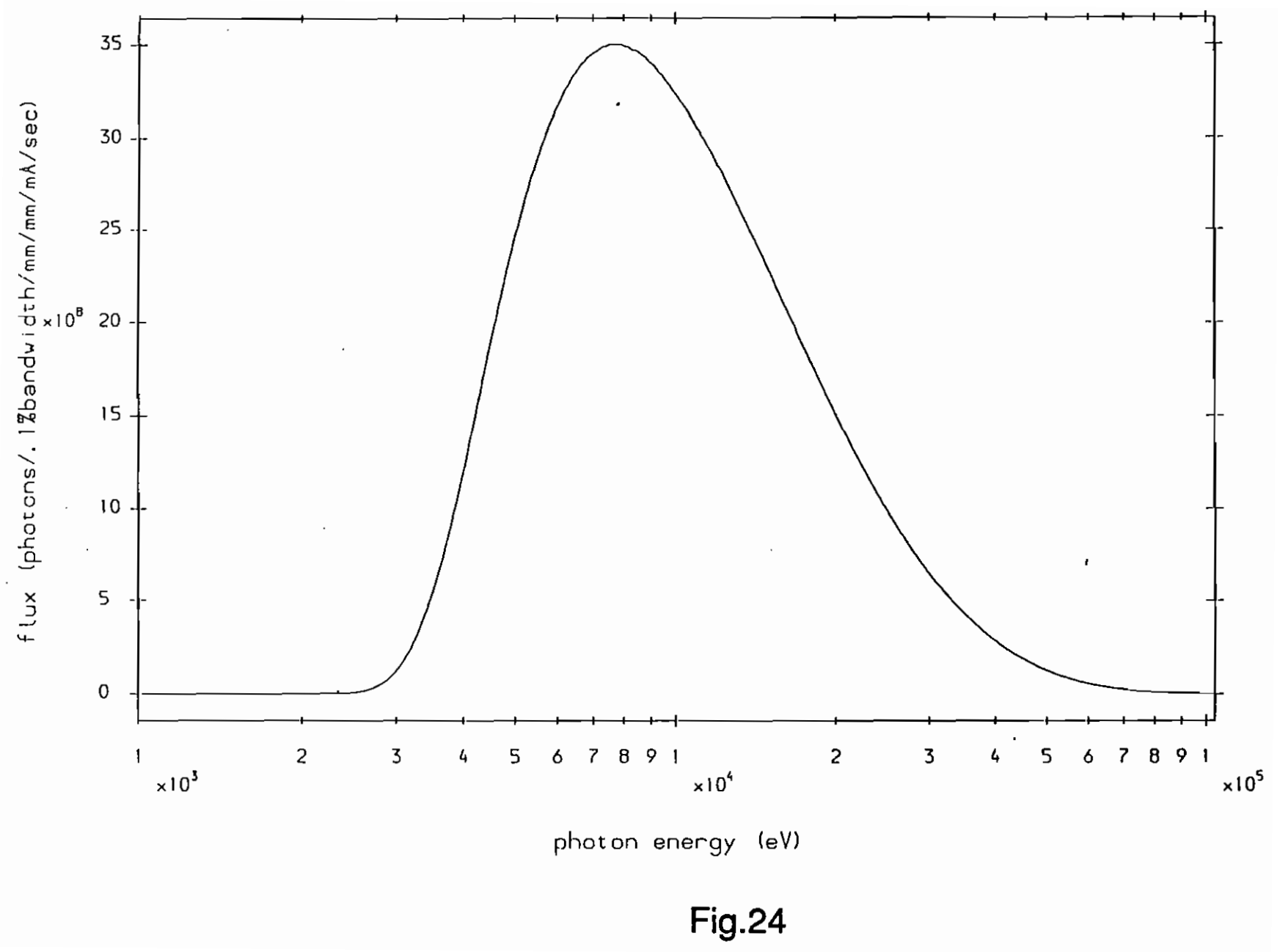
flux (photons/.1%bandwidth/mm/mm/mA/sec)
x10^8
35
30
25
20
15
10
5
0
1
2
3
4
5
6
7
8
9
1
2
3
4
5
6
7
8
9
1
x10^3
x10^4
x10^5
photon energy (eV)

Fig.24

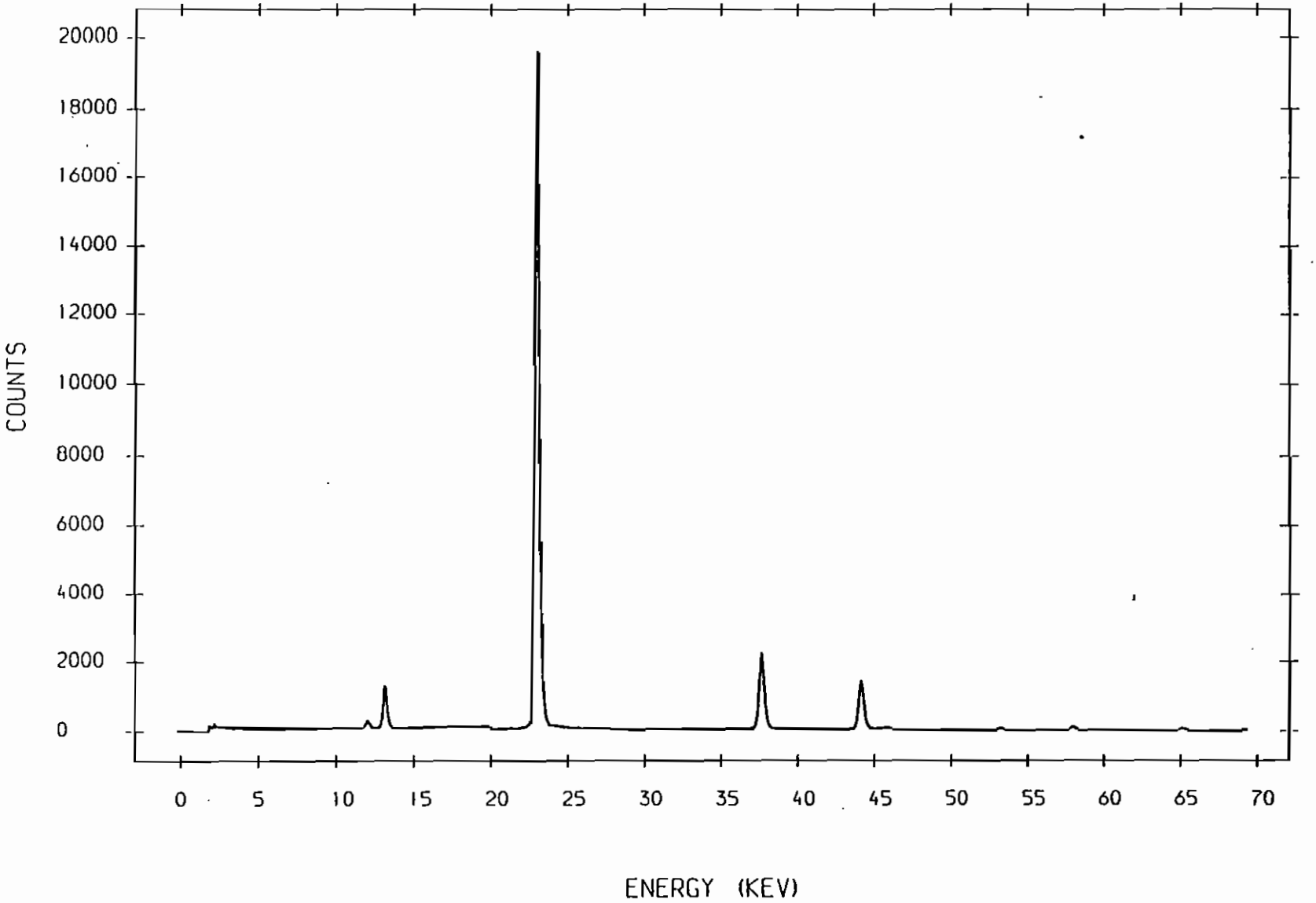
20000
18000
16000
14000
12000
10000
8000
6000
4000
2000
0
COUNTS
0
5
10
15
20
25
30
35
40
45
50
55
60
65
70
ENERGY (KEV)

Fig.25

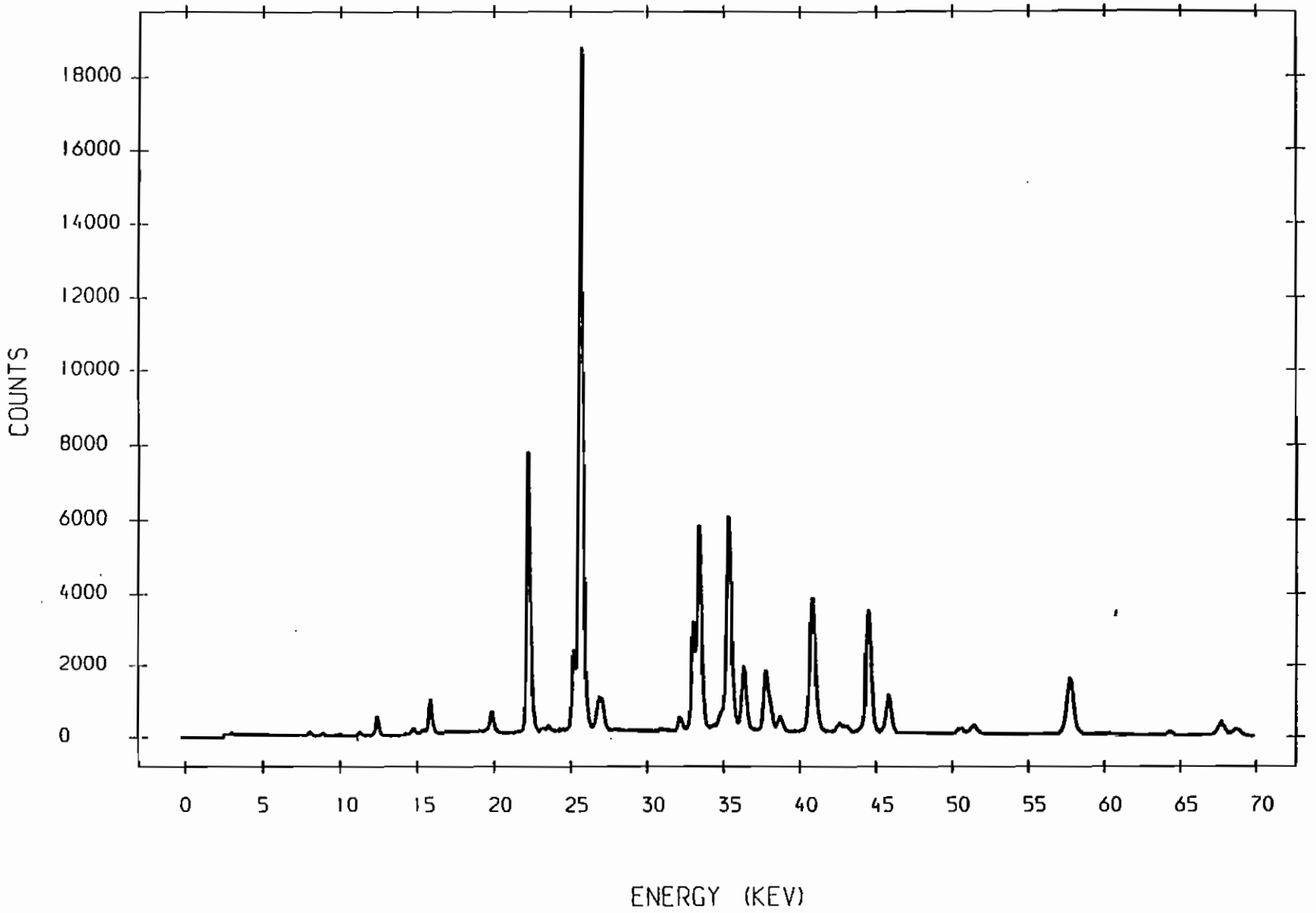
COUNTS
18000
16000
14000
12000
10000
8000
6000
4000
2000
0
0
5
10
15
20
25
30
35
40
45
50
55
60
65
70
ENERGY (KEV)

Fig.26

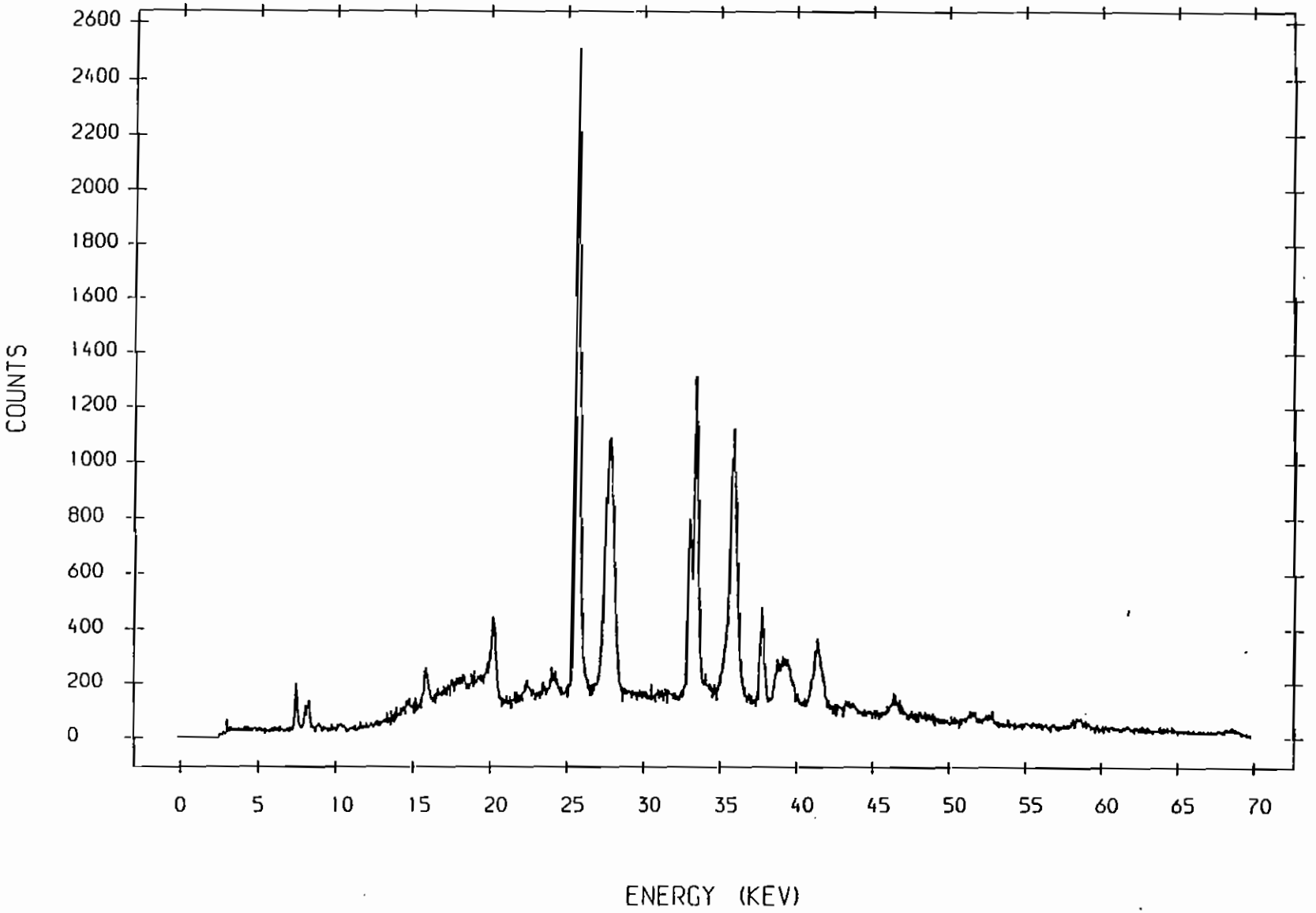
COUNTS
2600
2400
2200
2000
1800
1600
1400
1200
1000
800
600
400
200
0
0
5
10
15
20
25
30
35
40
45
50
55
60
65
70
ENERGY (KEV)

Fig.27

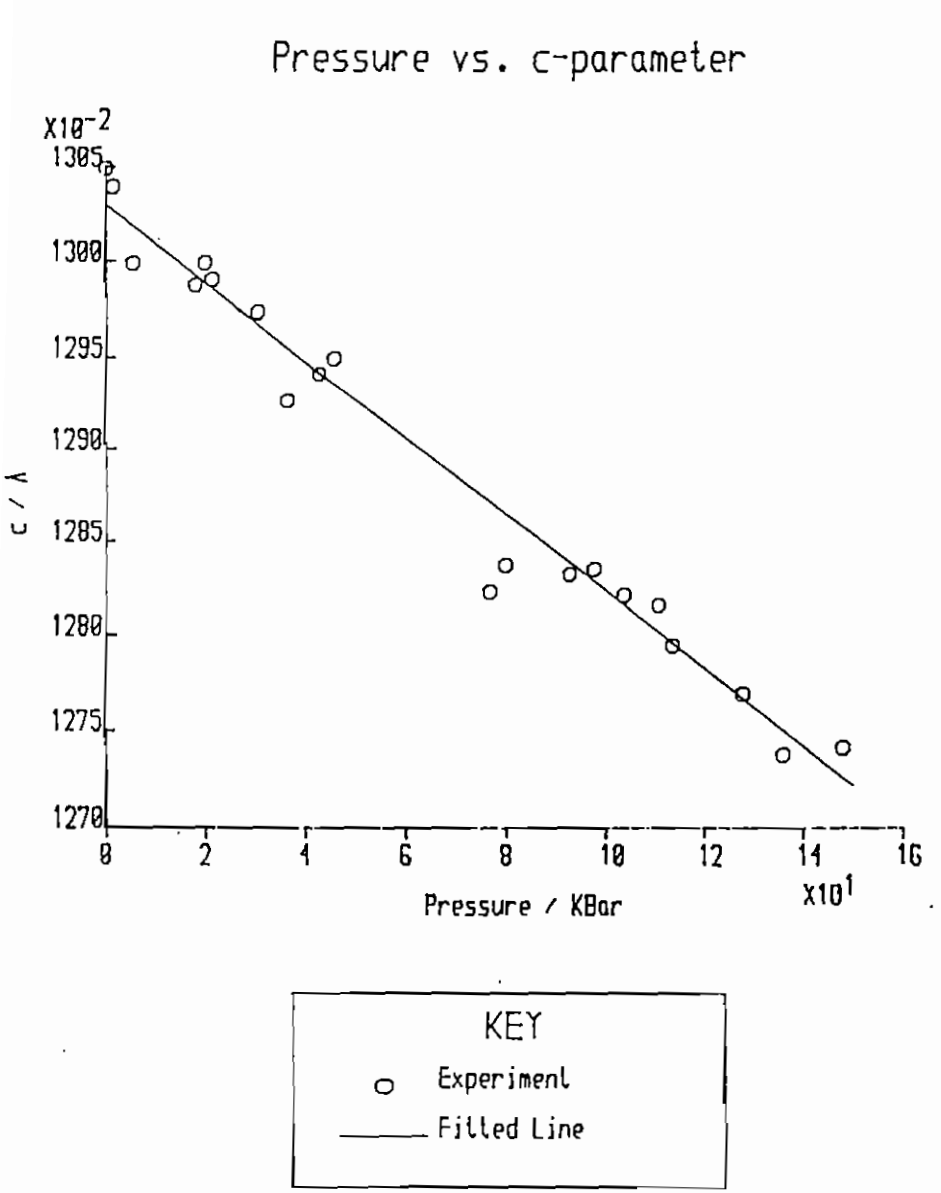
Pressure vs. c-parameter
X10-2
1305
1300
1295
1290
1285
1280
1275
1270
c / Å
0
2
4
6
8
10
12
14
16
X10¹
Pressure / KBar
KEY
Experiment
Filled Line

Fig.28

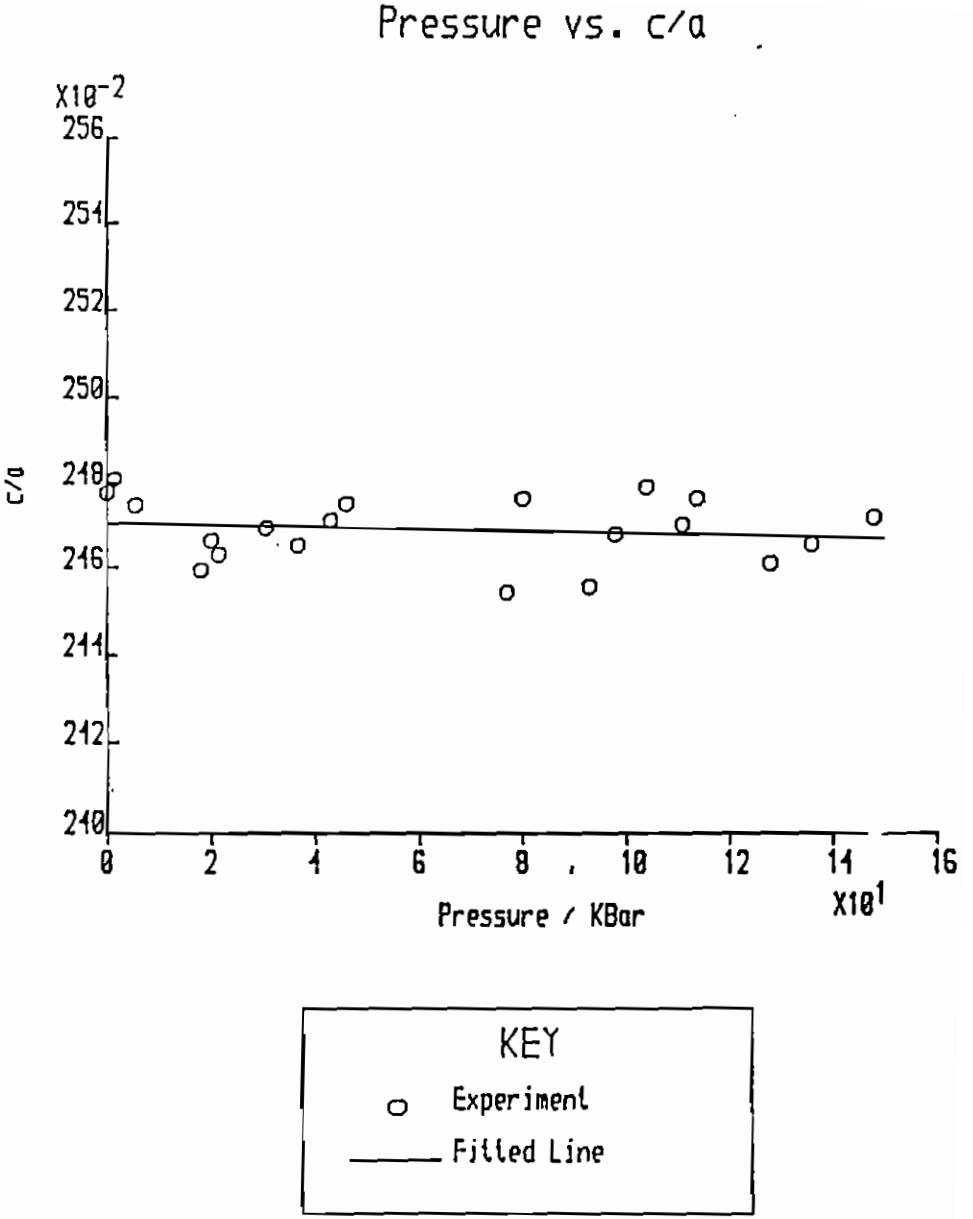
Pressure vs. c/a
X10-2
256
254
252
250
248
246
244
242
240
c/a
0
2
4
6
8
10
12
14
16
X10¹
Pressure / KBar
KEY
Experiment
Filled Line

Fig.29

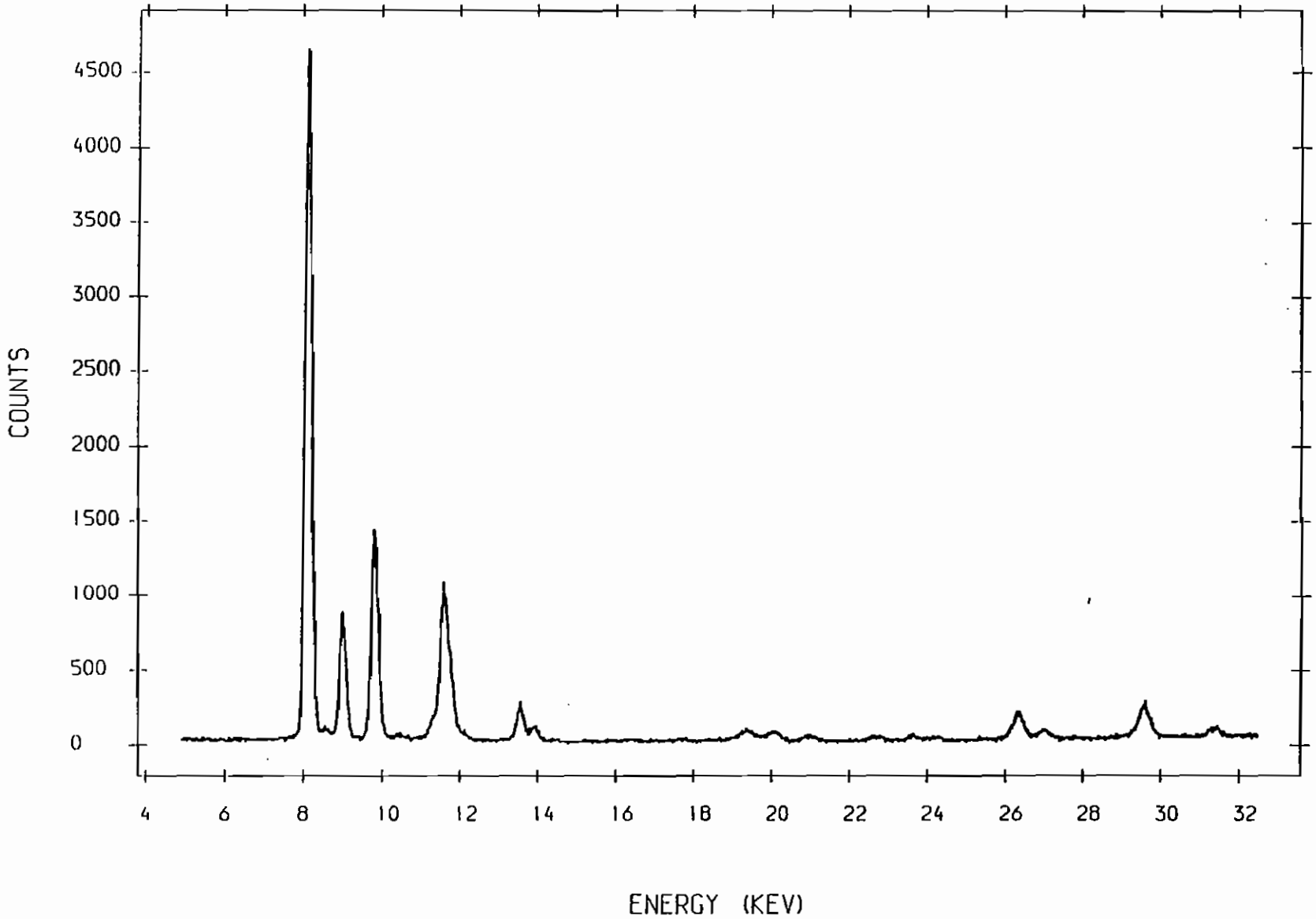
COUNTS
4500
4000
3500
3000
2500
2000
1500
1000
500
0
4
6
8
10
12
14
16
18
20
22
24
26
28
30
32
ENERGY (KEV)

Fig.30

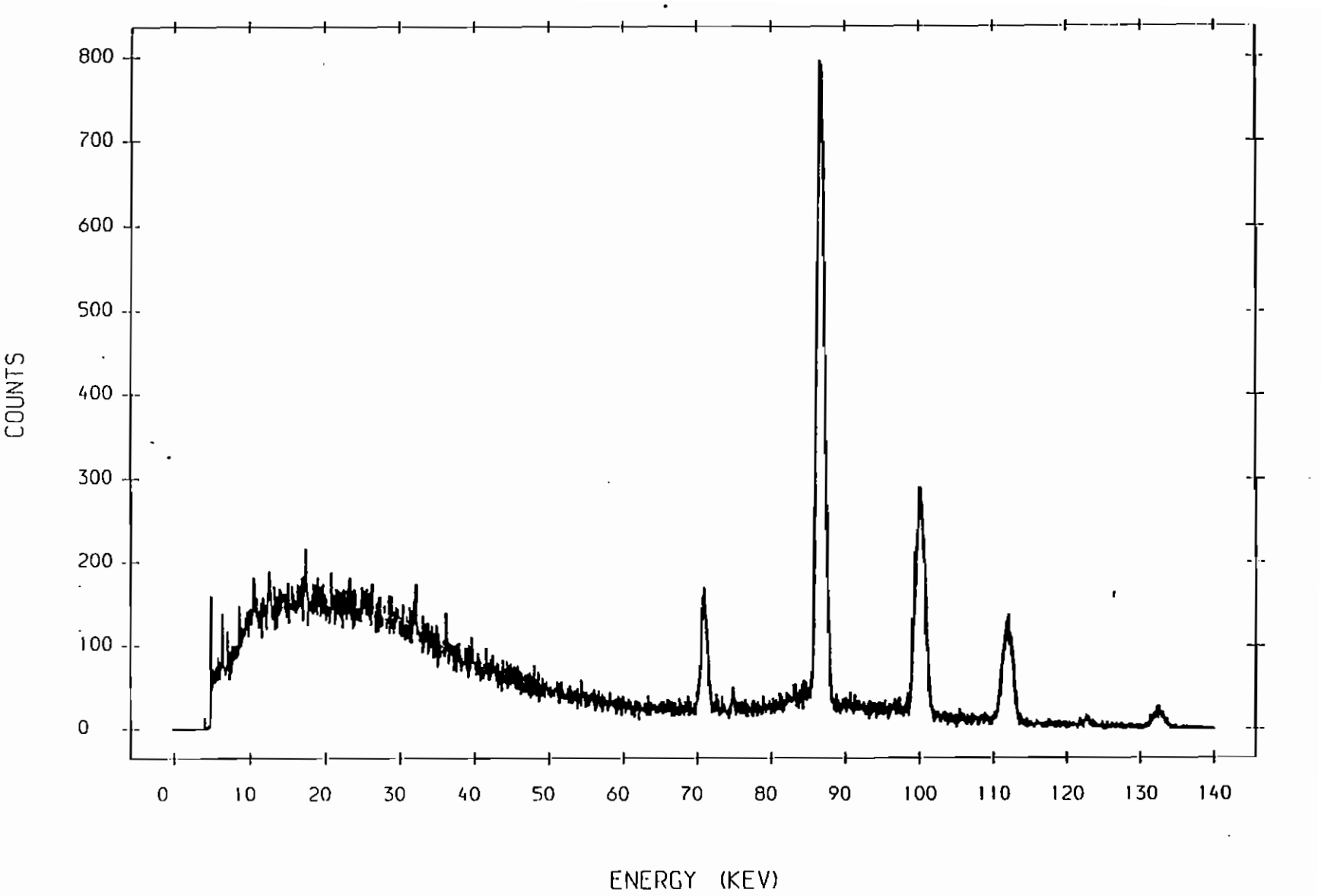
800
700
600
500
400
300
200
100
0
COUNTS
0
10
20
30
40
50
60
70
80
90
100
110
120
130
140
ENERGY (KEV)

Fig.31